

# A Rotational Motion Perception Neural Network Based on Asymmetric Spatiotemporal Visual Information Processing

Bin Hu, Shigang Yue, *Member, IEEE*, and Zhuhong Zhang

**Abstract**—All complex motion patterns can be decomposed into several elements, including translation, expansion/contraction, and rotational motion. In biological vision systems, scientists have found that specific types of visual neurons have specific preferences to each of the three motion elements. There are computational models on translation and expansion/contraction perceptions; however, little has been done in the past to create computational models for rotational motion perception. To fill this gap, we proposed a neural network that utilizes a specific spatiotemporal arrangement of asymmetric lateral inhibited direction selective neural networks (DSNNs) for rotational motion perception. The proposed neural network consists of two parts—presynaptic and postsynaptic parts. In the presynaptic part, there are a number of lateral inhibited DSNNs to extract directional visual cues. In the postsynaptic part, similar to the arrangement of the directional columns in the cerebral cortex, these direction selective neurons are arranged in a cyclic order to perceive rotational motion cues. In the postsynaptic network, the delayed excitation from each direction selective neuron is multiplied by the gathered excitation from this neuron and its unilateral counterparts depending on which rotation, clockwise (cw) or counter-cw (ccw), to perceive. Systematic experiments under various conditions and settings have been carried out and validated the robustness and reliability of the proposed neural network in detecting cw or ccw rotational motion. This research is a critical step further toward dynamic visual information processing.

**Index Terms**—Asymmetric lateral inhibition, directional columns, direction selective neurons, multiplication, rotation selective neuron, spatiotemporal computation, visual motion perception.

## I. INTRODUCTION

FOR most animals, visual perception plays the most important role for their survival. With efficient visual perception, animal actively perceives and captures useful

Manuscript received May 14, 2016; accepted May 29, 2016. This work was supported in part by the EU Seventh Framework Programme under Grant EYE2E/269118, Grant HAZCEPT/318907, and Grant LIVCODE/295151, in part by the National Science Foundation of China under Grant 61563009, and in part by the Horizon 2020 Project under Grant STEP2DYNNA/691154. (*Corresponding author: Shigang Yue*.)

B. Hu is with the College of Computer Science and Technology, Guizhou University, Guiyang 550025, China, and also with the School of Computer Science, University of Lincoln, Lincoln LN6 7TS, U.K. (e-mail: csuhubin@163.com).

S. Yue is with the School of Computer Science, University of Lincoln, Lincoln LN6 7TS, U.K. (e-mail: syue@lincoln.ac.uk).

Z. Zhang is with the College of Big Data and Information Engineering, Guizhou University, Guiyang 550025, China (e-mail: sci.zhzhang@gzu.edu.cn).

Color versions of one or more of the figures in this paper are available online at <http://ieeexplore.ieee.org>.

Digital Object Identifier 10.1109/TNNLS.2016.2592969

visual information about its external environments, such as an object's motion, shape, color, and so on, and converges them to the higher cerebral cortex for decision making. Among these visual information perceptions, motion perception is particularly important for the survival of most animal species in critical moments, such as to detect predators or to hunt for prey.

In the real world, the diversity of motion patterns can be decomposed into three types of basic motion elements or patterns, including translation, expansion/contraction, and rotational motion [1], [2]. These basic motion patterns play important roles in motion synthesis, for instance, a moving wheel contains translation and rotational motion.

In biological vision systems, scientists have found specific types of visual neurons have specific preferences to each of the three motion elements. For example, Hubel and Wiesel [3] discovered that simple, complex, and hypercomplex neuron types demonstrate orientation and velocity sensitivity characteristics. In visual neurophysiological studies, three types of neurons have been found in the dorsal part of medial superior temporal (MSTd), ventral intraparietal area, anterior region of the superior temporal polysensory area, and area 7a in the primate brain [4]–[18]—these neurons are translation, rotation, and expansion/contraction neurons, which preferentially respond to translation, rotation, or expansion/contraction motion patterns.

For rotation selective neurons in biological vision systems, a number of studies have found its presence in the cerebral cortex of the primate. For example, Leinonen [19] reported neurons in Posterior Area 7 positively responding to rotational stimuli in the awake monkey. Rizzolatti *et al.* [20] found similar neurons in the premotor cerebral cortex. Sakata *et al.* [5], [6] found those rotation-sensitive neurons in the posterior parietal association cerebral cortex (area PG) of the alert monkey. Saito *et al.* [21] found that some neurons in the medial superior temporal (MST) area of the anesthetized monkey were sensitive to rotary movement. Tanaka and Saito [8] analyzed the functional properties of the rotation selective neurons with the direction and expansion/contraction neurons of MSTd in more detail, and proposed that a circular arrangement of movement directions in the wide-field stimuli was essential for the activation of rotation neurons. Duffy and Wurtz [10], [11] also found that some neurons in the MSTd are sensitive to circular motion of optic flow stimuli, and further discovered that the MSTd neurons respond not only to translation, expansion/contraction, or rotation but also often to two or all

three of these motions. Rotation selective (RS) neurons have also been found in other animal species, such as human and birds. Cavanagh and Favreau [22], Petersik *et al.* [23], Hershenson [24], Wall *et al.* [25], and Morrone *et al.* [26] found that the human visual system contains the rotation detectors by demonstrating rotational motion aftereffects. Koban and Cook [27] and Nankoo *et al.* [28] found that pigeons are most sensitive to rotational motion in their research. All the above research studies suggest the existence of the rotation selective neurons in the biological visual pathways. However, the underlying mechanism of how a biological vision system perceives rotational motion remains unclear. There were a few appropriate computational models that focused on rotational motion perception in the past, let alone systematic investigation on the performance of such a rotation selective neural model.

On the other hand, constructing a rotation selective neural network based on the updated information revealed in neurophysiological studies may not only provide a building block for future artificial vision systems but also help to further understand biological vision systems.

In this paper, we propose a bio-plausible rotational motion perception visual neural network based on the latest discoveries in neurophysiological studies. It makes use of asymmetrical lateral inhibited presynaptic neural networks and spatiotemporal circular arrangements as postsynaptic structure to achieve rotational motion perception. The proposed neural network models, for clockwise (cw) and counter ccw, respectively, are validated with systematic tests under various conditions.

The rest of this paper is organized as follows. In Section II, related work will be reviewed. In Section III, the proposed neural networks are described in detail. In Section IV, experiments are carried out to test the performance of the new neural network system in different conditions.

## II. RELATED WORK

In this section, we describe the related work from qualitative models in neurophysiology study, approaches with classical neural networks, and quantitative models to the studies that link rotational to direction selective neurons.

Up to now, motion perceptions of translation and expansion/contraction have been modeled and tested (see [29]–[33]). However, a few quantitative rotational perception models have been proposed, alongside several classical neural network models as detailed in the following. To our knowledge, there is no bio-plausible quantitative model for rotational motion perception in the literature up to date.

### A. Qualitative Models in Neurophysiology Study

In the study of cerebral neurophysiology, Saito *et al.* [21] proposed a neural network that makes use of partially overlapping compartments in an MST receptive field. This model needs a special surround effect in middle temporal (MT) neurons to prevent many compartments from being activated simultaneously. In Duffy and Wurtz's model [11], the local rotation and expansion of the velocity field is derived and summed up across space to get invariant responses.

This algorithm requires that MT neurons be selective to local rotation and expansion/contraction, which is generally not the case [7]. Orban *et al.* [34] combined physiological recording and modeling techniques and proposed a computational model using Gaussian-shaped tuning function. However, the value of the standard deviation in the Gaussian-shaped tuning function affects the position invariance feature of this model; a larger standard deviation value will make the model increasingly selective to the location of the center of rotation.

### B. Quantitative Models for Rotational Motion Perception

In quantitative models, King *et al.* [35] designed a neural network that consists of multilayered velocity sensitive sensory cells organized in a locally connected fashion; however, the neural network cannot distinguish the direction of the rotational motion (cw or ccw). Guo *et al.* [36] proposed a model for the perception of rotational motion based on Reichardt's correlation motion detector array, Kohonen's self-organized feature map, and Schuster-Wagner's oscillating neural network on how these neural networks are trained and the performance of the network is not clear.

The above two models demonstrated periodic responses to rotational motion with different structures—the functionality similar to our presynaptic part that can be excited in a sequential way to rotational motion. Without postsynaptic part for specific rotational motion perception, the above two models are hard to compare with our model due to their incompleteness.

### C. Classical Neural Network Approaches

With different classical neural networks and learning rules, many other researchers have also proposed approaches to detect rotational motion, such as those in [37]–[42]. However, these classical neural networks need to learn from or train with a large number of rotational motion samples in order to work properly. Like other classical neural networks, their robustness and underlying biological origin are questionable.

### D. Research Links Directional to Rotation Selective Neurons

In the neurophysiological study of rotational motion perception, Sakata *et al.* [6], [43], [44] and Tanaka and Saito [8] reported the functional properties of RS neurons in the posterior parietal association cerebral cortex of a monkey. They found the fact that a pair of spots moving around the fixation point is as effective as a solid bar rotating in their experiment. This phenomenon suggests that the changing motion direction is more important than the changing object orientation. Therefore, they made a point that the continuous change of motion direction in rotational motion is the only difference that distinguishes rotary from linear movement [6], [43], which is supported by Caplovitz and Tse's [45] study on retinotopic area V3A in the human. This suggests that a rotational perception model could be created if it can detect the continuous change of motion direction of an object.

These instantaneous motion directions of an object could be sensed by direction selective neurons.

Neurophysiological studies have revealed that direction selective neurons widely exist in different animal species, including invertebrates and vertebrates, such as fly, beetle, locust, zebrafish, cat, and rabbit [29], [46]–[55]. There are many ways to construct a direction selective neural network (DSNN) model [29], [31], [56]. In recent years, one type of whole-field DSNN based on the asymmetric lateral inhibitory mechanism was modeled [57]–[60], and a large number of experimental results suggested that it is robust in an object's motion direction perception.

### E. Proposed Bio-Plausible Quantitative Model

In this paper, we propose a new quantitative model to perceive rotational motions mainly on the frontoparallel plane. Based on the asymmetrically inhibited direction selective neuron models, the proposed hierarchical visual neural network has a mechanism of spatiotemporal coherence for rotational motion perception. In this visual neural network, different asymmetric lateral inhibitory mechanisms are used to perceive 16 motion directions. Similar to the arrangement of directional columns in the mammalian's cerebral cortex (see [61]), the 16 direction selective neurons are arranged in a specific order, forming a cyclic structure to perceive the continuous change of motion direction. The excitation of each direction selective neuron is delayed with one time step, and then multiplied with the gathered excitation from the neuron and its unilateral counterparts depending on which rotary direction to perceive. Since the gathered excitation is from only *one specific side*, this rotational motion perception neural network (RMPNN) can respond to either ccw or cw rotational motion.

## III. ROTATION PERCEPTION VISION SYSTEM

In the study of biological visual system, Morrone *et al.* [62] provided psychophysical evidence for the existence of neural mechanisms in human vision and revealed that rotational or radial motion perception includes two stages of visual processing: 1) motion-sensitive neurons in V1 respond best to local translation and 2) many neurons in MST have large receptive fields tuned to rotational or radial motion. However, they mentioned only such two phrases from the psychophysics' point of view and did not investigate how neural systems percept rotational motions.

In this study, an RMPNN to perceive rotational motion should be based on their presynaptic and postsynaptic counterparts. The RMPNN includes two types of networks, one is ccwRMPNN, which responds to the ccw rotational motion, and the other is cwRMPNN, which responds to the cw rotational motion. We chose ccwRMPNN as an example to present its structure and principle in this paper. The schematic illustration of a ccwRMPNN is given in Fig. 1(a).

As shown in the Fig. 1(a), the ccwRMPNN consists of two main parts: the first is presynaptic networks that are 16 whole field DSNNs to perceive translation motion cues, and the second is the postsynaptic network that focuses on

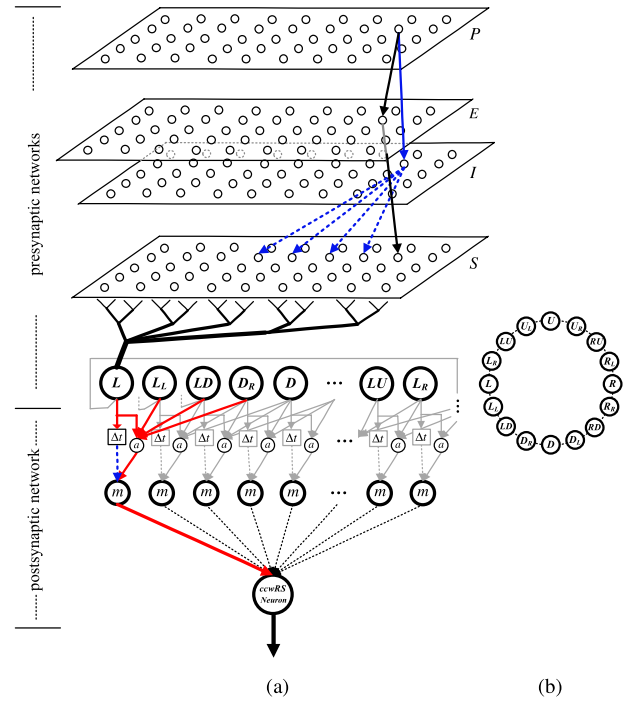


Fig. 1. (a) Schematic illustration of the ccwRMPNN. (b) Schematic illustration of the arrangement of the 16 direction selective neurons in the ccwRMPNN.

the perception of rotational motion. Details of the two parts will be given in the following sections.

### A. Presynaptic Networks for Motion Direction Perception

The presynaptic networks of ccwRMPNN contains the whole field DSNNs, which are based on [57]–[60], and they can perceive different visual motion cues on the frontoparallel plane in the field of view. According to the difference of lateral inhibition regions, the 16 *direction selective neurons* in the DSNNs are divided into three types. For all of them, they have the similar structure except different inhibition regions. Therefore, we choose three typical direction selective neurons in each type: the left neuron *L*, the upper left direction selective neuron *LU*, and the right region of the left direction selective neuron *LR* as examples to illustrate their information processing mechanism.

The left direction selective neuron (*L* neuron) prefers the left direction moving edges on the frontoparallel plane; its presynaptic neural network is illustrated in Fig. 1(a) (top). As shown in Fig. 1(a), there are four layers and one neuron in the presynaptic network of an *L* neuron: a *P* layer, an *E/I* layer, an *S* layer, and an *L* neuron. The function of each layer and the direction selective neuron *L* will be described in detail in the consecutive sections.

*1) P Layer:* The first layer of the *L* neuron neural network is the photoreceptor *P* cells. These cells are arranged in matrix form. In this layer, each photoreceptor cell collects the luminance  $L_f$  of each pixel in the input image at frame  $f$  and calculates the change of luminance  $P_f$  between two sequentially adjacent frames of the video images and then excitation of these photoreceptor cells as output

results of this layer. The output of each cell in this layer is given by

$$P_f(x, y) = \sum_i^{n_p} p_i P_{f-i}(x, y) + \text{abs}(L_f(x, y) - L_{f-1}(x, y)) - \xi_{\text{noise}} \quad (1)$$

where  $P_f(x, y)$  is the change of luminance that corresponds to pixel  $(x, y)$  at frame  $f$ ;  $x$  and  $y$  are the pixel coordinates;  $p_i \in (0, 1)$  is the persistence coefficient, which is defined by  $p_i = (1 + e^{\mu i})^{-1}$ ,  $\mu \in (-\infty, +\infty)$ ;  $n_p$  represents the maximum time steps (or number of image frames) the persistence of the luminance change can last;  $L_f$  and  $L_{f-1}$  are the luminance, the subscript  $f$  denotes the current frame and the subscript  $f - 1$  denotes the previous frame; and  $\xi_{\text{noise}}$  is the threshold of signal noise.

2) *I/E Layer*: The output of the  $P$  cells is the input to the next two separated type's of cells in the *E/I* layers, respectively. In these two layers, the first type of cells is excitatory cells, through which excitation is passed directly to their retinotopic counterpart in the third layer of the network, the *S* layer; the second type of cells is inhibition cells, which pass inhibition to their retinotopic counterpart's neighboring cells in the *S* layer. In both *E/I* layers, cells are arranged in matrix form.

The excitation and the inhibition from a  $P$  cell pass to its counterpart in the *E* layer and the *I* layer directly. The input excitation  $E(x, y)$  in an *E* cell and the input inhibition  $I(x, y)$  in an *I* cell have the same value as that in the corresponding  $P$  cell.

3) *S Layer*: Cells in the *S* layer receive excitation and inhibition from the *E/I* layers, and these cells are also arranged in matrix form. The output excitation of an *E* cell is the same as its input excitation and passes to its counterpart in the *S* layer directly. However, the output inhibition of an *I* cell is its input inhibition delay one time step (or image frame) and passes to its retinotopic counterpart's left-side neighboring cells (or passes to its counterpart's all neighboring cells except the left side, if an *L* cell should prefer leftward movements only) in the *S* layer up to  $n$  cells away. Therefore, the strengths of excitation and gathered inhibition to a cell in the *S* layer are, respectively

$$E_f(x, y) = P_f(x, y) \quad (2)$$

$$I_f^L(x, y) = \sum_{i=1}^{n_{\text{inh}}} P_{f-1}(x+i, y) w_I(i) \quad (3)$$

where  $E_f(x, y)$  and  $I_f^L(x, y)$  are the excitation and the inhibition to the same cell in the *S* layer at  $(x, y)$ , respectively, the superscript  $L$  denotes the specific direction selective neuron that prefers the left direction motion;  $n_{\text{inh}}$  is the inhibition radius, i.e., a maximum number of cells in the *I* layer that spread their inhibitions to the same cell in the *S* layer at  $(x, y)$ ; and  $w_I(i) \in [0, 5.5]$  is the local inhibition weight, which controls the neighboring inhibition strength. Therefore, with an appropriate inhibition radius from the right side with one frame delay, the *S* cells' excitation caused by the left moving edges can be eliminated or weakened sharply in this layer.

Then, the excitation strength of these cells gathered in an *S* cell is

$$S_f(x, y) = E_f(x, y) - I_f^L(x, y) W_I \quad (4)$$

where  $S_f(x, y)$  is the specific cell excitation in the *S* layer at  $(x, y)$  and  $W_I$  is the global inhibition weight, which controls the overall inhibition strength.

In the *S* layer, only for those cells whose excitation exceeds the threshold  $T_{\text{rs}}$  will be transmitted to the *L* neuron. Therefore, if the excitation of a cell less than the threshold  $T_{\text{rs}}$  is set to zero; otherwise, it remains unchanged

$$\tilde{S}_f(x, y) = \begin{cases} 0, & \text{if } S_f(x, y) < T_{\text{rs}} \\ S_f(x, y), & \text{if } S_f(x, y) \geq T_{\text{rs}} \end{cases} \quad (5)$$

4) *Left Direction Selective Neuron*: The input excitation of the *L* neuron is summed by the excitation of all cells in the *S* layer

$$\text{Sum}_f^L = \sum_{x=1}^{n_c} \sum_{y=1}^{n_r} \text{abs}(\tilde{S}_f(x, y)) \quad (6)$$

where  $\text{Sum}_f^L$  is the summed excitation of the *L* neuron, and  $n_c$  and  $n_r$  are the total number of cells in a row and a column in the *S* layer, respectively.

The summed excitation of the *L* neuron is then processed as

$$V_f^L = 2 \times \left( 1 - \left( 1 + e^{-\frac{\text{Sum}_f^L}{n_{\text{rc}}}} \right)^{-1} \right) \quad (7)$$

where  $n_{\text{rc}}$  is the total number of the cells in the *S* layer. According to (6),  $\text{Sum}_f^L$  is greater than or equal to zero, so *L* neuron excitation  $V_f^L \in [0 \sim 1.0]$ .

As for the spatiotemporal processing mechanism described above, the stimuli generated by the object moving to the left will make *L* neuron excitation maximum in the 16 direction selective neurons. Other direction selective neurons, for example, the right direction selective neuron (*R*), the up direction selective neuron (*U*), and the down direction selective neuron (*D*), share the same mechanism in forming their direction selective sensitiveness.

5) *Other Types of Direction Selective Neurons*: Besides the above *L*, *R*, *U* and *D* direction selective neurons, two types of direction selective neurons, diagonal visual motion and neighborhood direction visual motion, are also used in this paper. There are four neurons to perceive the diagonal visual motions: *LU* (left-up), *LD* (left-down), *RU* (right-up), *RD* (right-down), and eight neurons to perceive the neighborhood direction visual motions: *L<sub>L</sub>* (left side of *L*), *L<sub>R</sub>* (right side of *L*), *D<sub>L</sub>* (left side of *D*), *D<sub>R</sub>* (right side of *D*), *R<sub>L</sub>* (left side of *R*), *R<sub>R</sub>* (right side of *R*), *U<sub>L</sub>* (left side of *U*), and *U<sub>R</sub>* (right side of *U*).

We take *LU* and *L<sub>L</sub>* neurons as examples to describe the direction perception principle of the two types of neurons. The differences among *LU*, *L<sub>L</sub>*, and *L* are the regions of inhibition direction in the *S* layer. For the *LU* neuron, the inhibition from an *I* cell passes to its retinotopic counterpart's left-up side neighboring cells in the *S* layer up to  $n$  cells away with

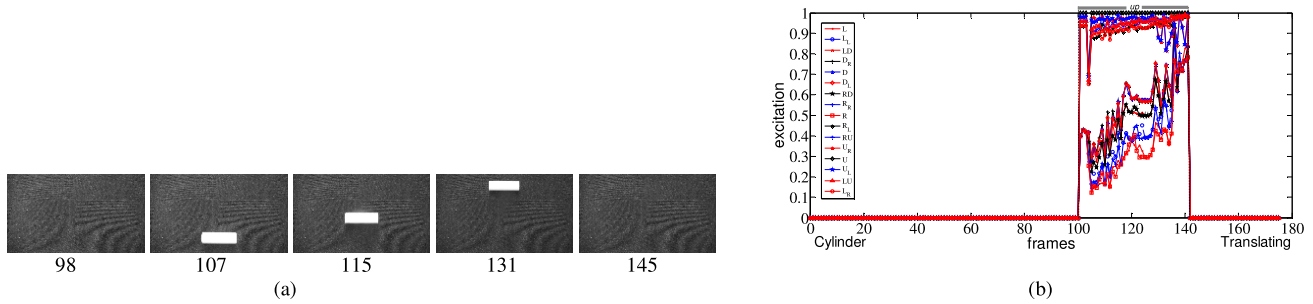


Fig. 2. Example of video sequences of the direction selective neuron process with an up moving white cylinder on a carpeted office floor. (a) Sample images of the video sequence. The frame number is indicated under each image. (b) Excitation of the 16 direction selective neurons.

one image frame delay. The gathered strength of inhibition to a cell in this  $S$  layer is

$$I_f^{LU}(x, y) = \sum_{j=1, i=j}^{n_{\text{inh}}} P_{f-1}(x + i, y + j) w_I(i, j). \quad (8)$$

Similarly, for  $L_L$  neuron, the gathered strength of inhibition to a cell in the  $S$  layer is

$$I_f^{L_L}(x, y) = \sum_{i=2, j=1, i>j}^{n_{\text{inh}}} P_{f-1}(x + i, y - j) w_I(i, j). \quad (9)$$

For other diagonal and neighborhood direction selective neurons, the inhibition gathered by a cell in the  $S$  layer can be illustrated in the similar way.

*6) Arrangement of the 16 Direction Selective Neurons:* In the cerebral cortex of the mammalian, neurons with a similar axis of motion preference exist in the form of directional columns, which may represent directions continuously from  $0^\circ$  to  $360^\circ$  [61]. Similarly, the 16 direction selective neurons in RMPNN's presynaptic network are arranged in this specific order and forming a cyclic structure to perceive a different motion direction [as indicated in Fig. 1(b)]. Consequently, at any given time, the whole presynaptic networks are able to perceive the changing motion directions of an object and pass these motion cues to their postsynaptic network for further processing.

To demonstrate the functionality of these presynaptic networks in detecting motion direction, one video sequence showing an up moving white cylinder on a carpeted office floor was processed by the 16 DSNNs. As shown in Fig. 2, the responded excitation from the direction selective neuron  $U$  and other neurons close to  $U$  are significantly greater than that from other direction selective neurons. This experiment reassured that the visual motion cues can be extracted by these DSNNs for further processing.

### B. Postsynaptic Network for Rotational Motion Perception

The schematic illustration of ccwRMPNN's postsynaptic networks is shown in Fig. 1(a) (top). In RMPNN's postsynaptic network, the excitation of each direction selective neuron is delayed with one time step and then multiplied with the gathered excitation from the neuron and its unilateral counterparts depending on which rotary direction to perceive

(e.g., right side of ccwRMPNN and left side of cwRMPNN). The postsynaptic networks consist of two layers and one specific rotational motion selective neuron: an excitation gathering operation layer, an excitation multiplication operation layer, and a ccw RS (ccwRS) neuron.

Expression  $\Gamma_f$  is the 16 direction selective neuron excitation vector in ccwRMPNN's presynaptic networks

$$\Gamma_f = (V_f^L V_f^{L_L} V_f^{LD} V_f^{D_R} V_f^D \dots V_f^{L_R})^T \quad (10)$$

where the subscript  $f$  denotes time step (or video frame number) and  $V_f^L, V_f^{L_L}, V_f^{LD}, V_f^{D_R}, V_f^D, \dots, V_f^{L_R}$  are the excitations of the 16 direction selective neurons.

Excitation of each direction selective neuron that spreads into the postsynaptic network is determined by a spiking mechanism. When the excitation of a direction selective neuron  $V_f^i$  exceeds threshold  $T_e$ , one internal spike occurs inside this neuron

$$S_f^{\text{Transpike}}(i) = \begin{cases} 1, & \text{if } V_f^i > T_e \text{ and } V_f^i > 0 \\ 0, & \text{otherwise} \end{cases} \quad (11)$$

If there are  $m_{\text{sp}}$  spikes in  $m_{\text{ts}}$  time steps ( $m_{\text{sp}} \leq m_{\text{ts}}$ ) inside the same direction selective neuron  $q$  ( $q \in \{L, \dots, L_R\}$ ), a nonrotation is perceived. Simultaneously, only those excitations exceeding or equal to threshold  $T_e$  will be transmitted to their retinotopic counterpart in the postsynaptic network

$$\tilde{V}_f(i) = \begin{cases} 0, & \text{if } V_f(i) < T_e \text{ or } \sum_{j=0}^{m_{\text{ts}}-1} S_{f-j}^{\text{Transpikes}}(q) \geq m_{\text{sp}} \\ V, & \text{if } V_f(i) \geq T_e \text{ and } \sum_{j=0}^{m_{\text{ts}}-1} S_{f-j}^{\text{Transpikes}}(q) < m_{\text{sp}} \end{cases} \quad (12)$$

$$V_f(i) \in \{V_f^L, V_f^{L_L}, V_f^{LD}, V_f^{D_R}, V_f^D, \dots, V_f^{L_R}\}.$$

In this formula, the threshold  $T_e$  is defined by the following:

$$T_e = \text{MAX}_{2\text{nd}i=1,\dots,n} \{V_f(i)\} \quad (13)$$

where  $\text{MAX}_{2\text{nd}i=1,\dots,n} \{V_f(i)\}$  represents the submaximum in the array  $V_f(i)$ .

Therefore, the output excitation vector of the 16 direction selective neurons spread into the postsynaptic network is

$$\tilde{\Gamma}_f = (\tilde{V}_f^L \tilde{V}_f^{L_L} \tilde{V}_f^{LD} \tilde{V}_f^{D_R} \tilde{V}_f^D \dots \tilde{V}_f^{L_R})^T. \quad (14)$$

For a stationary object, all elements in the vector  $\tilde{\Gamma}_f$  are zero. When the object is in motion, however, a few elements in  $\tilde{\Gamma}_f$  could be greater than zero. The function of each layer and the ccwRS neuron will be described in the following in detail.

*1) Excitation Gathering Operation Layer:* The first layer of the postsynaptic network is the excitation gathering operation layer, which consists of 16 identical cells  $a$ . Each  $a$  cell receives excitations from its ccw side neighboring direction selective neurons in the upper layer up to  $m_{\text{neighbor}}$  neurons away. Therefore, the strengths of excitation to an  $a$  cell in this layer are

$$A_f(i) = \underset{j=0, \dots, m_{\text{neighbor}}}{\text{MAX}} \{ \tilde{\Gamma}_f(i+j) \} \quad (15)$$

where  $A_f(i)$  is the gathered excitation of an  $a$  cell,  $i$  denotes the index of an  $a$  cell, and the subscript  $f$  denotes the current frame;  $m_{\text{neighbor}}$  is the maximum number of direction selective neuron in the upper layer that spread excitation to an  $a$  cell in this layer; and  $\tilde{\Gamma}_f(i+j)$  is the  $(i+j)$ th index direction selective neuron excitation in the upper layer. From the above,  $A_f(i)$  is equal to either zero or the gathered excitations from the  $(i)$ th to the  $(i+m_{\text{neighbor}})$ th direction selective neurons in the current frame.

*2) Excitation Multiplication Operation Layer:* The postsynaptic network's second layer is the excitation multiplication operation layer; it is composed of 16 identical multiplication operator cells  $m$ . These  $m$  cells receive the excitation from its retinotopic counterpart in the 16 direction selective neurons with one frame delay and then multiply this excitation with the other excitation transmitted by its retinotopic counterpart in the excitation gathering operation layer immediately. Therefore, the gathered excitations to an  $m$  cell in this layer are

$$M_f(i) = A_f(i) \times V_{f-1}(i) \quad (16)$$

where  $M_f(i)$  is the multiplication result of an  $m$  cell's excitation,  $i$  denotes the index of the 16  $m$  cells, the subscript  $f$  denotes the current frame, and  $f-1$  denotes the previous frame. From the above,  $M_f(i)$  is greater than or equal to zero.

*3) ccwRS Neuron:* Finally, 16  $m$  cell excitations are converged to ccwRS neuron. The strength of the converged excitations to the ccwRS neuron is

$$\kappa_f = \underset{i=1, \dots, n}{\text{MAX}} \{ M_f(i) \} \quad (17)$$

where  $\kappa_f$  is the input excitation of ccwRS neuron, the subscript  $f$  denotes the current frame, and  $n$  is the number of the  $m$  cells.

The output excitation of the ccwRS neuron is regulated by a spiking mechanism, i.e., when the input excitation  $\kappa_f$  exceeds a threshold  $T_s$ , an internal spike inside the ccwRS neuron is produced and otherwise remains silent

$$S_f^{\text{RSNspike}} = \begin{cases} 1, & \text{if } \kappa_f > T_s \\ 0, & \text{otherwise.} \end{cases} \quad (18)$$

If there are  $n_{\text{sp}}$  successive spikes occurring inside the ccwRS neuron, a ccw rotational motion is perceived, and the ccwRS neuron will produce its output excitation immediately. If  $\kappa_f \geq \gamma_{\text{am}}$  ( $\gamma_{\text{am}} = 0.9$ ), the output excitation  $\tilde{\kappa}_f = \kappa_f$ ; otherwise,  $\tilde{\kappa}_f$

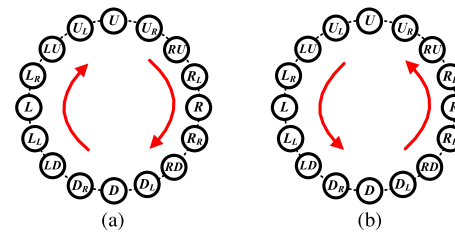


Fig. 3. Only difference between cwRMPNN and ccwRMPNN is the opposite excitation transmission direction sequence of the 16 direction selective neurons. (a) cwRMPNN. (b) ccwRMPNN.

is encouraged iteratively by the following equation till it is greater than or equal to  $\gamma_{\text{am}}$ :

$$\tilde{\kappa}_f = \kappa_f \times \sigma^{\kappa_f - 1} \quad (19)$$

where  $\sigma$  is the excitation amplification factor. After being encouraged,  $\tilde{\kappa}_f \in [0.9 \sim 1]$ . Finally, the output excitation of the ccwRS neuron  $F_{\text{ccwRS}}$  is

$$F_{\text{ccwRS}} = \begin{cases} \tilde{\kappa}_f, & \text{if } \sum_{f_s}^f s_f^{\text{RSNspike}} \geq n_{\text{sp}} \\ 0, & \text{otherwise.} \end{cases} \quad (20)$$

The threshold  $n_{\text{sp}}$  is

$$n_{\text{sp}} = n_{ts} + \sum_{f^1=f_s}^f \left( m_{f^1}^s(k) - \frac{m_{(f^1-1)}^s(k)!}{m_{(f^1-2)}^s(k)!} \right) \quad (21)$$

where  $k (k \in \{L, \dots, L_R\})$  denotes the index of the direction selective neuron that produces a spike at frame  $f^1$  and  $m_{f^1}^s(k) (0 \leq m_{f^1}^s(k) \leq m_{sp-1})$  is the total number of continuous spikes occurring inside the direction selective neuron  $k$  up to frame  $f^1$ . The  $m_{f^1}^s(k)$  can be summarized as

$$m_{f^1}^s(k) = \begin{cases} \sum_{i=0}^{m_{ts}-2} S_{f-1}^{\text{Transpike}}(k), & \text{if } f \geq f_s \\ 0, & \text{s.t. } f-i \geq f_s \\ & \text{otherwise} \end{cases} \quad (22)$$

where  $f_s$  denotes the first time step (or image frame) of the current time period when continuous spikes are occurring inside the ccwRS neuron.

### C. cw Rotational Motion Perception Neural Network

The structure of a cwRMPNN is the same as the above-described structure of a ccwRMPNN; however, the excitation gathering direction from these direction selective neurons is completely the opposite, as shown in Fig. 3. In ccwRMPNN, when a ccw rotational motion occurs, the excitations of direction selective neurons are successively transmitted in accordance with the ccw direction and the ccw rotational motion is perceived by the ccwRMPNN. However, a cwRMPNN will not respond to a cw rotational motion, unless its internal structure in gathering excitations is changed to an opposite way, i.e., to become a cwRMPNN (see Fig. 3).

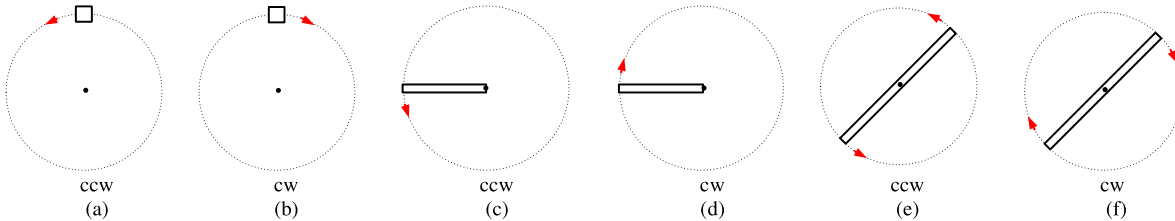


Fig. 4. Schematic illustrations of three types of objects' rotational motion patterns. (a) ccw rotating block. (b) cw rotating block. (c) ccw rotating half-bar. (d) cw rotating half-bar. (e) ccw rotating bar. (f) cw rotating bar. All video sequences are accessible at [http://www.ciluk.org/temp/05\\_TestVideos.zip](http://www.ciluk.org/temp/05_TestVideos.zip).

TABLE I  
PARAMETERS OF THE RMPNN

Name	Value	Name	Value
$p_i$	0	$\sigma$	0.5
$u$	0	$n_{inh}$	8~30
$w_I$	5.5	$m_{neighbor}$	3
$W_I$	1.7	$m_{sp}$	6
$T_{rs}$	12	$m_{ts}$	6
$n_{rc}$	11200	$n_{ts}$	8
$n_c$	140	$T_s$	0
$n_r$	80		

#### D. Parameters of the System

In this study, all experiments are executed on a Microsoft Windows Server 2008 with CPU/2.66G and RAM/4G and source codes are written in C++. In the simulation, each situation of the real scene video sequences of rotational motion is taken at 30 frames/s and the input frames to RMPNN are  $140 \times 80$  resolution grayscale images with an 8-b precision.

Based on the previous experimental studies [63], [57]–[60] and the current trials, the parameters of RMPNN are given in Table I. In these experiments, the direction selective neurons be used are the left selective neuron  $L$ , right selective neuron  $R$ , up selective neuron  $U$ , down selective neuron  $D$ , left-up selective neuron  $LU$ , left-down selective neuron  $LD$ , right-up selective neuron  $RU$ , right-down selective neuron  $RD$ , left side of the  $L$  selective neuron  $L_L$ , right side of the  $L$  selective neuron  $L_R$ , left side of the  $D$  selective neuron  $D_L$ , right side of  $D$  selective neuron  $D_R$ , left side of the  $R$  selective neuron  $R_L$ , right side of the  $R$  selective neuron  $R_R$ , left side of the  $U$  selective neuron  $U_L$ , and right side of the  $U$  selective neuron  $U_R$ . All the direction selective neurons used in each experiment are set in the same way except the inhibited directions.

In an RMPNN, each pixel in an input frame image has one corresponding cell in the  $P$  layer. Each input frame image is  $140 \times 80$  pixels; hence, there are 11200 cells in the  $P$  layer. It follows from this that there are 11200  $E$  cells and 11200  $I$  cells all shared by its 16 direction selective neurons; it has 179200  $S$  cells and 49 functional cells. Therefore, the total number of cells involved in RMPNN is 212849.

## IV. EXPERIMENTAL STUDY

In the study of the rotational motion selective neurons of the primate cerebral cortex, it was found these neurons respond well to the rotational motion of a *half-bar*, or a *bar*, or a *spot* [5], [6], [8], [10], [11], [21], [43]. Hence, we use several sets of video sequences, which are similar to those rotary objects in the above neurophysiological experiments, to test the performance of RMPNN. The schematics of different rotary objects are shown in Fig. 4.

In order to test the effectiveness and the robustness of RMPNN, we will use three sets of video sequences in our experiments. The first set of video sequences is computer-generated visual stimuli, which simulate the rotational motions of a *block*, a *half-bar*, and a *bar*, respectively (see Fig. 5). The second set of video sequences is recorded real scene video sequences about the rotational motions of a block, a half-bar, and a bar on the frontoparallel plane (see Fig. 7). The third set of video sequences is the boundary condition tests of the real objects' rotational motion scenes, each of them represents a special real scene (see Figs. 9, 12, 16, 19, 21, and 29). Two indicators were used as the main bases for evaluation in these tests to characterize the performance of RMPNN: the perception success rate of RS neuron and the false alarm rate of RS neuron.

#### A. Simulated Visual Stimuli Tests

In simulated visual stimuli tests, we use six groups of computer generated video sequences—each represents the simulated rotational motion of one of the three objects (see Fig. 5, a *block*, a *half-bar*, and a *bar*). The rotational objects are represented with  $7 \times 7$  pixel white block (306 frames),  $3 \times 30$  pixel white half-bar (304 frames), and  $3 \times 60$  pixel white bar (301 frames) conducting ccw or cw rotation against black background ( $140 \times 80$  pixels), respectively. In all these video sequences, the angular velocity of the object's rotational motion is 15.7 rad/s (see Fig. 5).

In the video sequence shown in Fig. 5(a), a white block initially remains stationary from frame 1 to frame 92, it then rotates at a constant angular velocity in ccw from frame 93 to frame 219 and finally remains stationary from frame 220 to the end. In the video sequence shown in Fig. 5(b), a white block remains stationary from frame 1 to frame 92 and rotates at a constant angular velocity in ccw from frame 93 to frame 217, and then remains stationary in the remaining video frames. Similarly, the video sequence in Fig. 5(c) and (d) simulates the ccw and cw rotational motion of a white half-bar; the video sequence in Fig. 5(e) and (f) simulates the ccw and cw

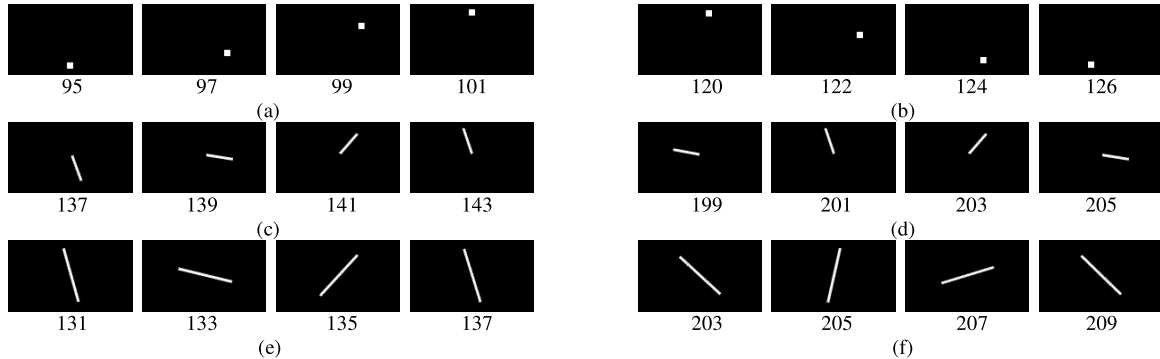


Fig. 5. Example frames from the simulated visual stimuli tests. Each video sequence is represented with four frames; the frame number is indicated under each image. (a) ccw rotating  $7 \times 7$  pixel white block. (b) cw rotating  $7 \times 7$  pixel white block. (c) ccw rotating  $3 \times 30$  pixel white half-bar. (d) cw rotating  $3 \times 30$  pixel white half-bar. (e) ccw rotating  $3 \times 60$  pixel white bar. (f) cw rotating  $3 \times 60$  pixel white bar. (For the detailed experimental settings and results, see Table II.)

TABLE II  
ROTATIONAL MOTION REGION PERCEPTIONS IN SIMULATED VISUAL STIMULI TESTS. (FOR THE EXPERIMENTS, SEE FIGS. 5 AND 6)

Video	The total of frames	Object type	Practical ccw rotational motion region (frames)	Practical cw rotational motion region (frames)	Angular velocity	RMPNN's ccw rotational motion region (frames)	RMPNN's cw rotational motion region (frames)	ccwRS neuron's success rate (%)	ccwRS neuron's false alarm rate (%)	cwRS neuron's success rate (%)	cwRS neuron's false alarm rate (%)
a	306	block	93-219	N/A	$15.7 \text{ rad/s}$	102-219	N/A	100	N/A	N/A	0
b	306	block	N/A	93-217	$15.7 \text{ rad/s}$	N/A	104-217	N/A	0	100	N/A
c	304	half-bar	92-216	N/A	$15.7 \text{ rad/s}$	101-216	N/A	100	N/A	N/A	0
d	304	half-bar	N/A	93-217	$15.7 \text{ rad/s}$	N/A	101-217	N/A	0	100	N/A
e	301	bar	93-213	N/A	$15.7 \text{ rad/s}$	102-213	N/A	100	N/A	N/A	0
f	301	bar	N/A	93-213	$15.7 \text{ rad/s}$	N/A	102-213	N/A	0	100	N/A

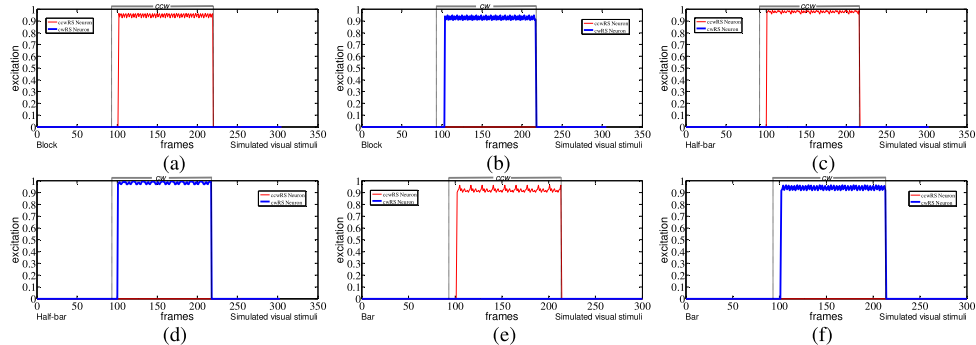


Fig. 6. Output curves of ccwRS neuron and cwRS neuron excitations. Each subgraph uniquely corresponds to the experimental results of the same identifier video sequence in Fig. 5. For example, (a) is the outputs of the ccwRS neuron and cwRS neuron in processing the simulated visual stimuli described in Fig. 5(a), and so is (b)–(f) respectively.

rotational motion of a white bar, respectively. The statistical results of these sequences are displayed in Table II.

Fig. 6 shows the test outputs of the RMPNN against these simulated image sequences. Table II indicates that the ccwRMPNN and cwRMPNN can correctly perceive the rotational motion for all simulated image sequences in these tests. From Fig. 6 and Table II, we found that the RMPNN worked very well for these simulated data sets.

### B. Real Scene Video Tests

We continue to test the RMPNN with recorded video sequences from real or physical scenes, where the three

objects, e.g., a black block, a black half-bar, and a black bar, were conducting ccw or cw rotational motion in a laboratory setting. First, we recorded two video sequences in which a regular black bar (60 mm in length and 5 mm in width) rotates around its center in ccw and cw, respectively, and then, we recorded two video sequences in which a black half-bar (30 mm in length, 5 mm in width) rotates around its one fixed end in ccw and cw, respectively. The rotational motion sequences of a block were edited from those of whole half-bar sequences, using video editing software (After Effects CS4, Adobe, USA). For each frame of the whole half-bar sequences, we erased almost the entire half-bar but leave its far end unchanged as the black block (see Fig. 7).

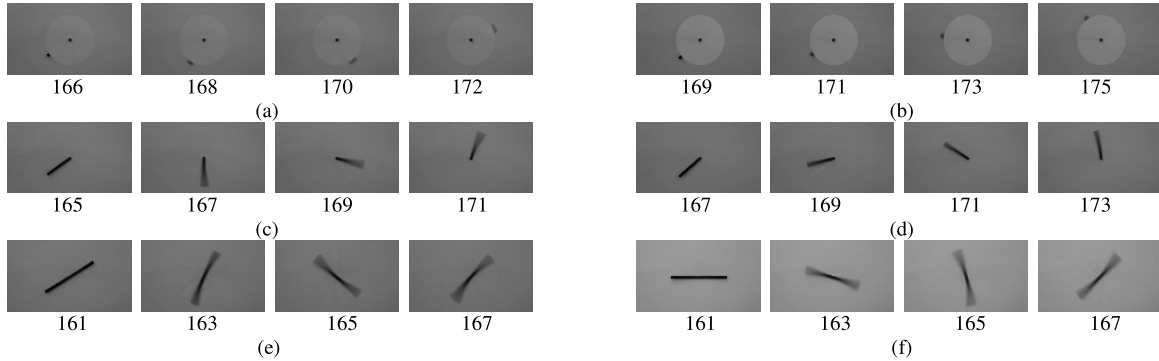


Fig. 7. Example frames from the real scene video tests. Each video sequence is represented with four frames; the frame number is indicated under each image. (a) ccw rotating black block. (b) cw rotating black block. (c) ccw rotating black half-bar. (d) cw rotating black half-bar. (e) ccw rotating black bar. (f) cw rotating black bar. (For the detailed experimental settings and results, see Table III.)

TABLE III  
ROTATIONAL MOTION REGION PERCEPTIONS IN REAL SCENE VIDEO TESTS. (FOR THE EXPERIMENTS, SEE FIGS. 7 AND 8)

Video	The total of frames	Object type	Practical ccw rotational motion region (frames)	Practical cw rotational motion region (frames)	Angular velocity	RMPNN's ccw rotational motion region (frames)	RMPNN's cw rotational motion region (frames)	ccwRS neuron's success rate (%)	ccwRS neuron's false alarm rate (%)	cwRS neuron's success rate (%)	cwRS neuron's false alarm rate (%)
a	561	block	167-507	N/A	23.55~17.13 rad/s	177-507	N/A	100	N/A	N/A	0
b	610	block	N/A	171-514	12.99 rad/s	N/A	186-514	N/A	0	100	N/A
c	561	half-bar	165-505	N/A	23.55~17.13 rad/s	174-505	N/A	100	N/A	N/A	0
d	610	half-bar	N/A	169-512	12.99 rad/s	N/A	181-512	N/A	0	100	N/A
e	596	bar	162-504	N/A	23.55~18.84 rad/s	171-504	N/A	100	N/A	N/A	0
f	699	bar	N/A	164-505	16.38~15.7 rad/s	N/A	175-505	N/A	0	100	N/A

In the video sequence shown in Fig. 7(a) (561 frames), a black block remains stationary from frame 1 to frame 166, after that it rotates at variable angular velocities (23.55–17.13 rad/s) in ccw from frame 167 to frame 507, and finally, it remains stationary from frame 508 to the end. In the video sequence Fig. 7(b) (610 frames), a black block holds stationary from frame 1 to frame 170, and it rotates at an angular velocity (12.99 rad/s) in cw from frame 171 to frame 514 and then keeps stationary from frame 515 to frame 610. In the video sequences of Fig. 7(c) and (d), the rotation pattern of a half-bar is the same as that of the block shown in Fig. 7(a) or (b) respectively. In video sequences of Fig. 7(e) and (f), the rotation pattern of a bar is similar to that of the block shown in Fig. 7(a) or (b), except the angular velocities 23.55–18.84 rad/s in Fig. 7(e) and 16.38–15.7 rad/s in Fig. 7(f). The statistical results of these sequences are displayed in Table III.

As illustrated in Fig. 8, we can clearly see that the proposed RMPNN works very well on these real scene video tests, although the rotation angular velocities of these objects are different.

### C. Boundary Condition Tests

In the following tests, the RMPNN will be challenged with several types of real scene video sequences under various conditions.

*1) Varied Inhibition Radius Tests:* In this section, we examine the effect of inhibition radius on the performance of RMPNN. During our experiment, we found that the motion perception of RMPNN was influenced by different inhibition radii. Too small inhibition radius will cause the incorrect perception of motion cues, while too large inhibition radius will lead to superfluous computing during its visual information processing. To effectively perceive the motion cues, an appropriate inhibition radius value should be set in the RMPNN.

Two recorded real scene videos were employed in these types of tests. One is the ccw rotational motion of *a half-bar* and the other is the ccw rotational motion of *a bar* (see Fig. 9). In the video sequence shown in Fig. 9(a) (478 frames), a half-bar rotates at an angular velocity (15.7 rad/s) in ccw from frame 1 to the end. In the video sequence shown in Fig. 9(b) (296 frames), a bar rotates at an angular velocity (20.93 rad/s) in ccw from the first frame to the last frame. During the tests, all parameters are fixed except the inhibition radius values in the RMPNN. We set six different inhibition radius values in each video test, respectively: 2, 4, 8, 16, 32, and 64 pixels.

Fig. 10 shows the output excitation of the RMPNN in this set of tests. From Fig. 10 (a)–(f), we can see that with the increasing inhibition radius, when the inhibition radius value is equal to or greater than 4 pixels, both the ccwRS neuron and the cwRS neuron can correctly perceive the rotational

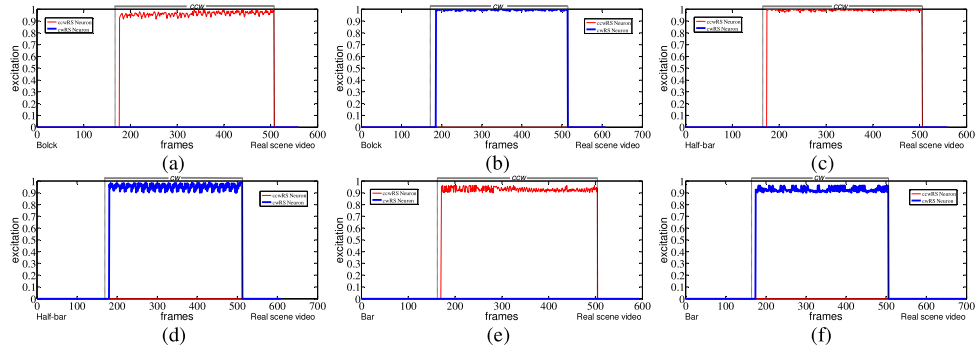


Fig. 8. Output curves of ccwRS neuron and cwRS neuron excitations. Each subgraph uniquely corresponds to the experimental results of the same identifier video sequence in Fig. 7.



Fig. 9. Example frames from the varied inhibition radius tests. Each video sequence is represented with four frames; the frame number is indicated under each image. (a) ccw rotating black half-bar. (b) cw rotating black bar.

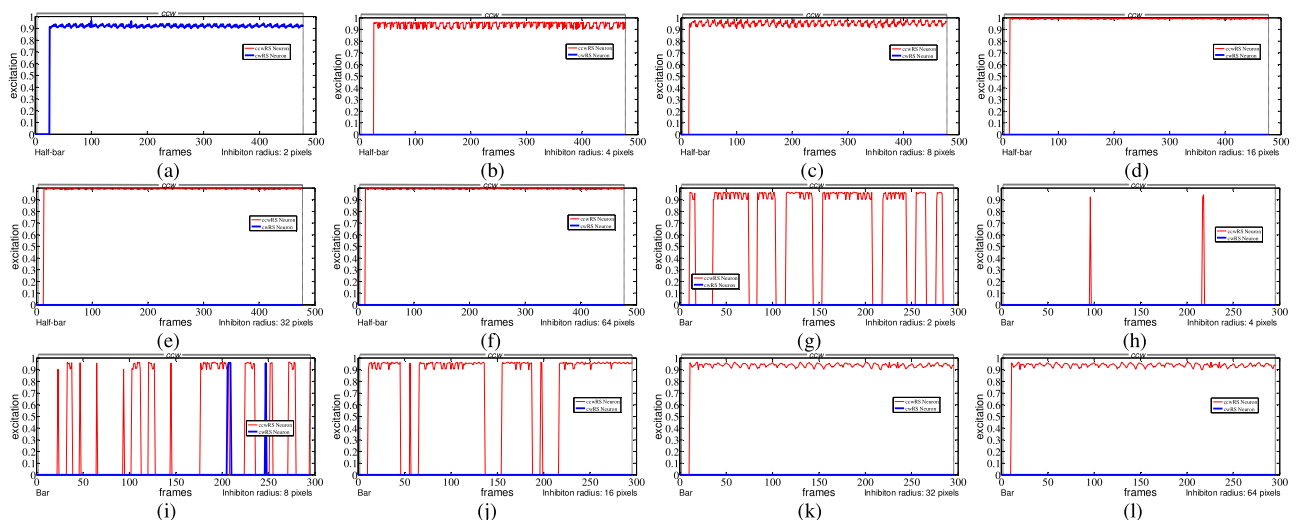


Fig. 10. Output curves of ccwRS neuron and cwRS neuron excitations. Each subgraph uniquely corresponds to a specific inhibition radius value in the test results of a video sequence in Fig. 9(a) or (b). (a) Half-bar:  $n_{inh} = 2$  pixels. (b) Half-bar:  $n_{inh} = 4$  pixels. (c) Half-bar:  $n_{inh} = 8$  pixels. (d) Half-bar:  $n_{inh} = 16$  pixels. (e) Half-bar:  $n_{inh} = 32$  pixels. (f) Half-bar:  $n_{inh} = 64$  pixels. (g) Bar:  $n_{inh} = 2$  pixels. (h) Bar:  $n_{inh} = 4$  pixels. (i) Bar:  $n_{inh} = 8$  pixels. (j) Bar:  $n_{inh} = 16$  pixels. (k) Bar:  $n_{inh} = 32$  pixels. (l) Bar:  $n_{inh} = 64$  pixels. Here  $n_{inh}$  is the inhibition radius.

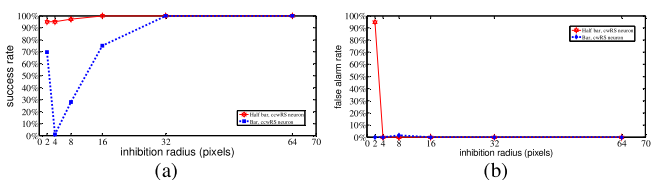


Fig. 11. CcwRS neuron perception success rate and cwRS neuron false alarm rate curves in the varied inhibition radius tests. (a) Perception success rates of the ccwRS neuron. (b) Perception false alarm rates of the cwRS neuron.

motion of a half-bar. From Fig. 10(g)–(l), we can find that when the inhibition radius value is varied within 2–16 pixels [Fig. 10(g)–(j)], the RMPNN cannot correctly perceive the

rotational motion of a bar in ccw, and even some incorrect response may appear, as shown in Fig. 10(i). With the growth of the inhibition radius value, while the inhibition radius is equal to or greater than 32 pixels, both the ccwRS neuron and the cwRS neuron can correctly perceive the rotational motion of the bar. Subsequently, we counted the perception success rate of the ccwRS neuron and the false alarm rate of the cw RS (cwRS) neuron in these different inhibition radius value tests and plotted rate–inhibition radius curves, as shown in Fig. 11. From these results, we found that an appropriate inhibition radius affect the performance of the RMPNN in perceiving rotational motion.

**2) Position Invariance and Varied Receptive Field Tests:** Position invariance is an important feature in the biological

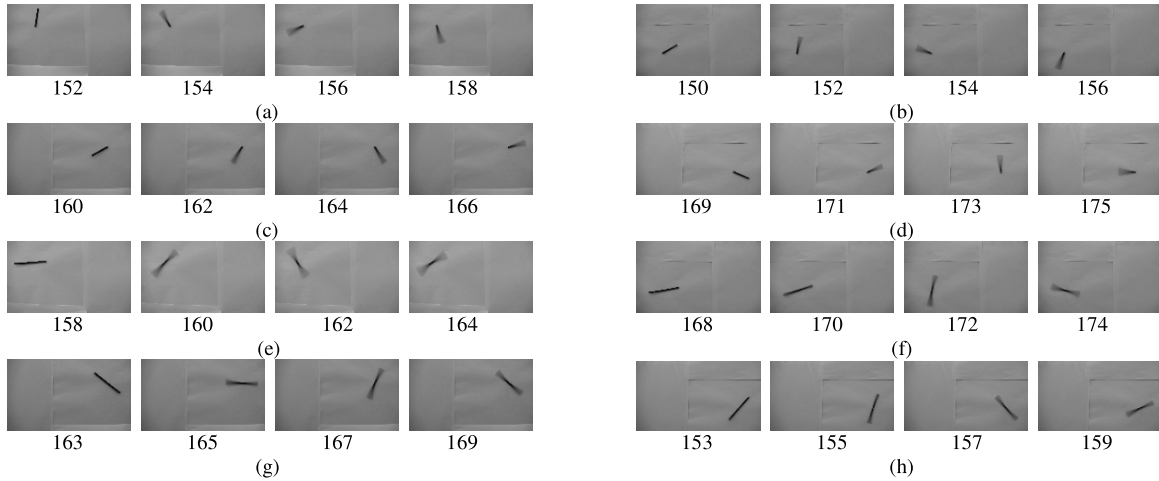


Fig. 12. Example frames from the position invariance and varied receptive field tests. Each video sequence is represented with four frames; the frame number is indicated under each image. (a) Half-bar: top-left area. (b) Half-bar: bottom-left area. (c) Half-bar: top-right area. (d) Half-bar: bottom-right area. (e) Bar: top-left area. (f) Bar: bottom-left area. (g) Bar: top-right area. (h) Bar: bottom-right area.

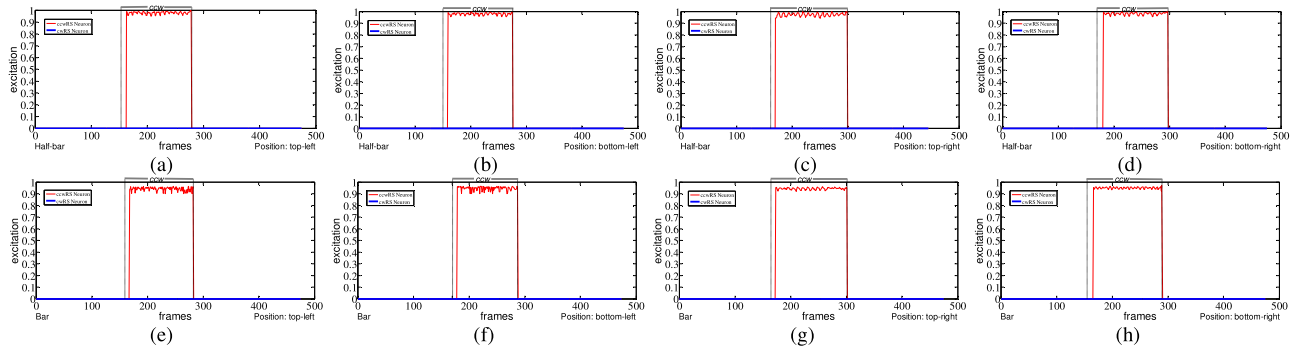


Fig. 13. Output curves of ccwRS neuron and cwRS neuron excitations. Each subgraph uniquely corresponds to the experimental results of the same identifier video sequence in Fig. 12.

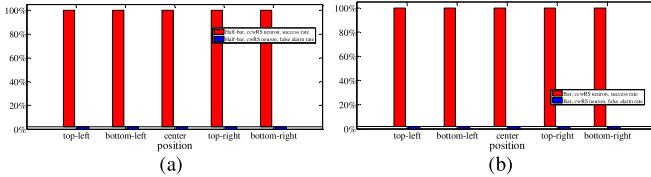


Fig. 14. ccwRS neuron perception success rates and cwRS neuron false alarm rate histograms in the position invariance and varied receptive field tests. (a) Perception success rates of the ccwRS neuron. (b) Perception false alarm rates of the cwRS neuron.

visual systems. Although an object in motion may appear at many different locations retinotopically, an animal can still perceive it correctly. This feature has been verified in neurophysiological experiments, e.g., Sakata *et al.* [43] found that the receptive fields of RS neurons in the cerebral cortex of the monkey are quite large, and a shift of the center of rotation within the receptive field does not cause a large difference in response.

In order to test the response of RMPNN to the rotational motion in different regions of the field of view, a set of experiments was designed. We recorded the rotational motion of a half-bar and a bar in ccw at different regions of the field of

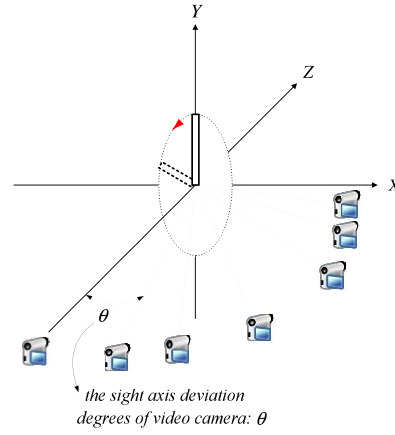


Fig. 15. Schematic illustration of the sight axis deviation tests.

view, respectively: top-left, bottom-left, top-right, and bottom-right (see Fig. 12). In these video sequences, the rotational motion patterns in ccw of the half-bar and the bar are similar to that of the previous simulated visual stimuli generated by a computer except for the difference in the rotation angular velocities (19.83–23.55 rad/s in this type of tests). In each

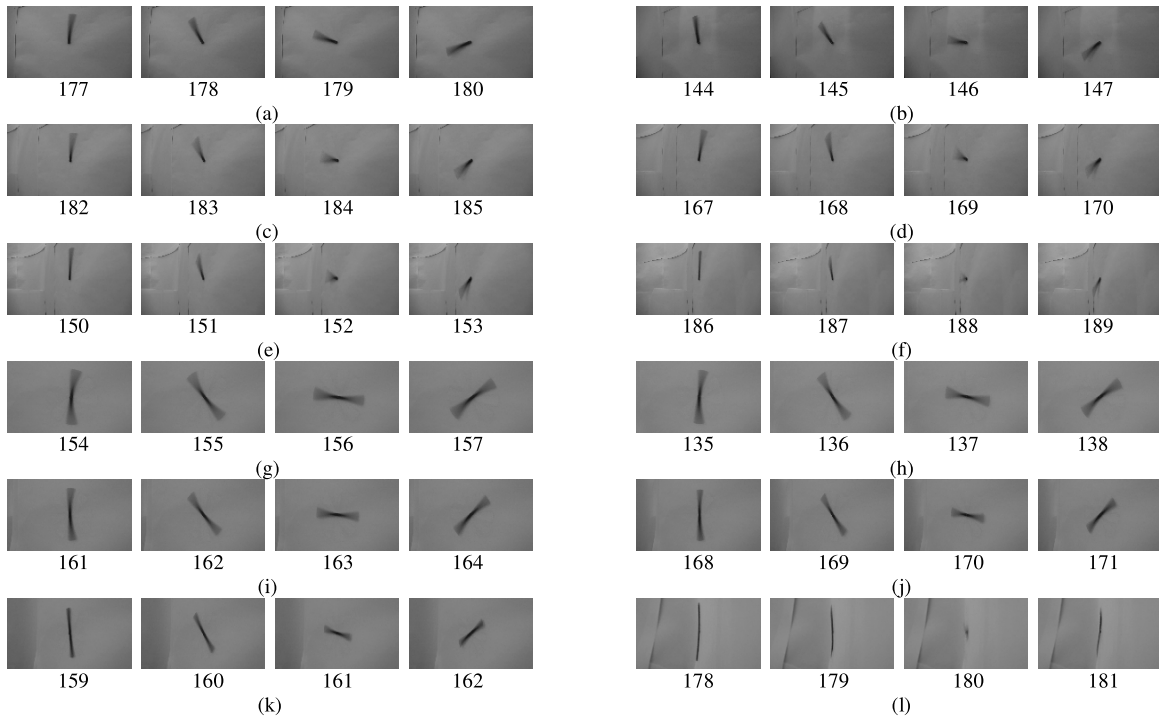


Fig. 16. Example frames from the sight axis deviation tests. Each video sequence is represented with four frames; the frame number is indicated under each image. (a) Half-bar:  $\theta = 15^\circ$ . (b) Half-bar:  $\theta = 30^\circ$ . (c) Half-bar:  $\theta = 45^\circ$ . (d) Half-bar:  $\theta = 60^\circ$ . (e) Half-bar:  $\theta = 75^\circ$ . (f) Half-bar:  $\theta = 85^\circ$ . (g) Bar:  $\theta = 15^\circ$ . (h) Bar:  $\theta = 30^\circ$ . (i) Bar:  $\theta = 45^\circ$ . (j) Bar:  $\theta = 60^\circ$ . (k) Bar:  $\theta = 75^\circ$ . (l) Bar:  $\theta = 85^\circ$ . Here  $\theta$  is the sight axis deviation degree of the video camera.

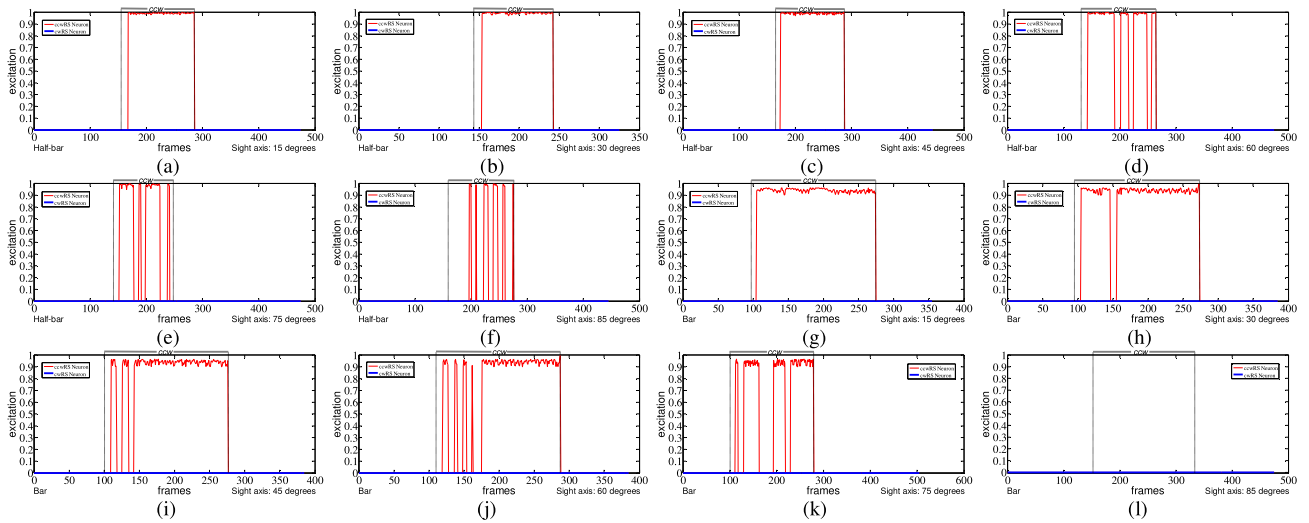


Fig. 17. Output curves of ccwRS neuron and cwRS neuron excitations. Each subgraph uniquely corresponds to the experimental result of the same identifier video sequence in Fig. 16.

video sequence, the object initially remains stationary for several seconds, and then rotates in ccw for a few seconds and finally stops rotating and remains stationary until the end of the video sequence. Then the RMPNN will be challenged by these video sequences.

The experimental results are shown in Figs. 13 and 14. The two charts show that RMPNN can correctly perceive the rotational motion of a half-bar and a bar, regardless of their different positions in the field of view. The results show that the proposed RMPNN is similar to the biological vision neural network—it also has the position invariance feature, which is compatible with the vector field hypothesis [11].

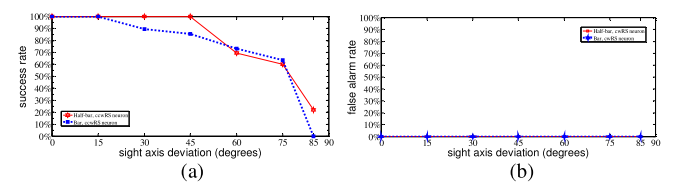


Fig. 18. ccwRS neuron perception success rate and cwRS neuron false alarm rate curves in the sight axis deviations tests. (a) Perception success rates of the ccwRS neuron. (b) Perception false alarm rates of the cwRS neuron.

3) *Sight Axis Deviation Tests:* In the above tests, the sight axis of video camera is perpendicular to the rotating plane of object, and the RMPNN responded well to these rotational



Fig. 19. Example frames of original video sequences from the varied intensity interference tests. Each original video sequence is represented with four frames; the frame number is indicated under each image. (a) Half-bar's ccw rotational motion mixed with interference. (b) Bar's ccw rotational motion mixed with interference.

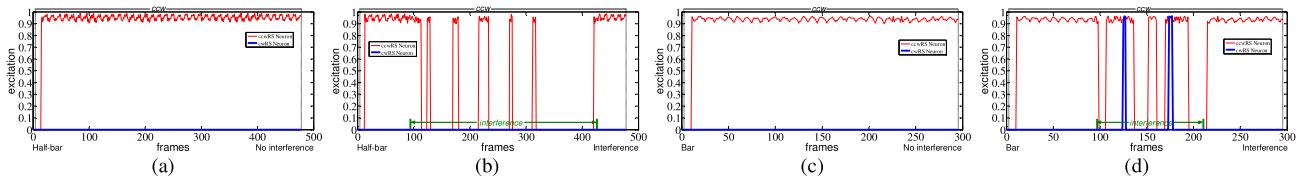


Fig. 20. Output curves of ccwRS neuron and cwRS neuron excitations. (a) Experimental result of the video sequence in Fig. 19 (a), but the interference was fully erased (i.e., a half-bar's ccw rotational motion without interference.). (b) Test result of the video sequence in Fig. 19(a). (c) Test result of the video sequence in Fig. 19(b), but the interference was fully erased (i.e., a bar's ccw rotational motion without interference). (b) Test result of the video sequence in Fig. 19(b).

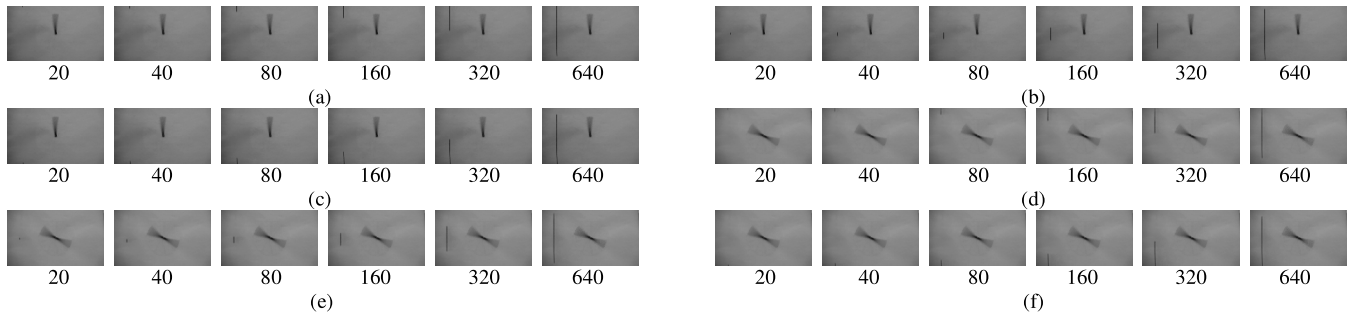


Fig. 21. Example frames from the varied intensity interference tests. By erasing different parts (upper, middle, and lower) of a cable, different intensity and swing amplitude interferences in different regions were formed. The resolution of each original video sequence is 720 pixels. The cable was partially erased and retained different height pixels in the three sections, respectively, and forming eight types of interference of the different cable lengths: 0 pixel (the cable disappears completely, i.e., noninterference), 20 pixels, 40 pixels, 80 pixels, 160 pixels, 320 pixels, 640 pixels, and 720 pixels [the full cable remains; see Fig. 19(a) and (b)]. The length of interference (i.e., the retained cable length in pixels) is indicated under each image. (a) Half-bar: interferences in the upper section. (b) Half-bar: interferences in the middle section. (c) Half-bar: interferences in the lower section. (d) Bar: interferences in the upper section. (e) Bar: interferences in the middle section. (f) Bar: interferences in the lower section.

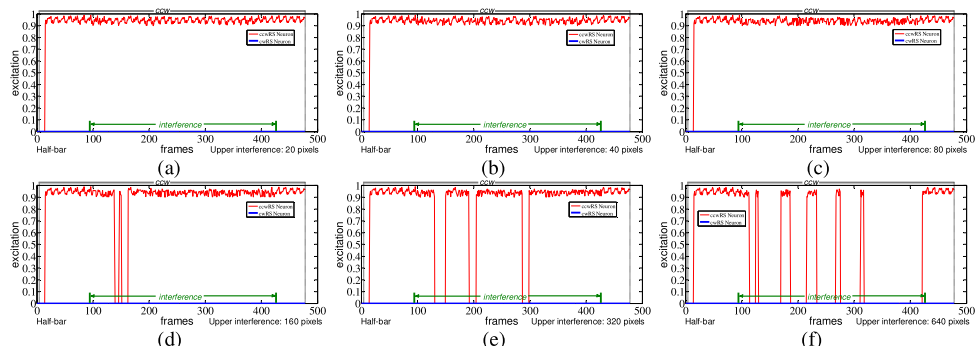


Fig. 22. Output curves of ccwRS neuron and cwRS neuron excitations. Each subgraph uniquely corresponds to the experimental results of a video sequence in Fig. 21(a). (a) Half-bar: 20-pixel swing cable interference. (b) Half-bar: 40-pixel swing cable interference. (c) Half-bar: 80-pixel swing cable interference. (d) Half-bar: 160-pixel swing cable interference. (e) Half-bar: 320-pixel swing cable interference. (f) Half-bar: 640-pixel swing cable interference.

motions of objects. However, rotational motion may happen in different planes. To test the impact of the sight axis deviation on the performance of RMPNN, we will use video sequences with different camera sight axis deviations on the horizontal plane (Fig. 15).

We progressively increased the horizontal deviation angle (on the  $x-z$  horizontal plane; see Fig. 15) between the

sight axis and the vertical line on the frontoparallel plane. In the adjacent video sequences of these tests, the camera's sight axis changed from the vertical line by  $15^\circ$  each time until it approached the parallel lines of the frontoparallel plane. As the sight axis deviation reached over  $75^\circ$ , we continued to increase  $10^\circ$  to make it at  $85^\circ$  for the final video sequences. The schematic of the sight axis deviation tests is shown

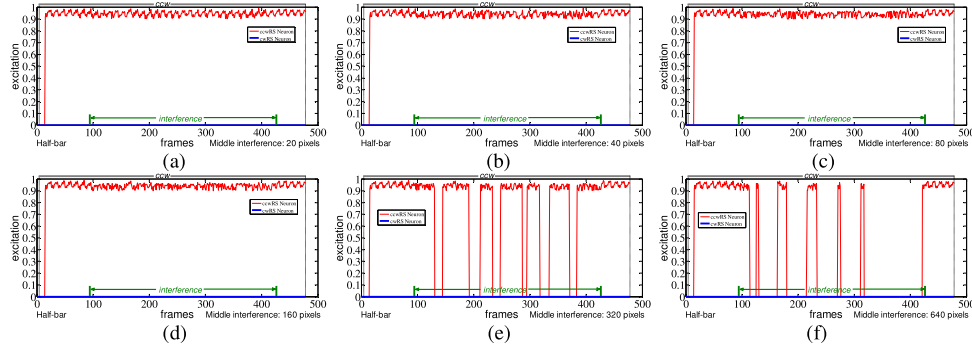


Fig. 23. Output curves of ccwRS neuron and cwRS neuron excitations. Each subgraph uniquely corresponds to the experimental results of a video sequence in Fig. 21(b). (a) Half-bar: 20-pixel swing cable interference. (b) Half-bar: 40-pixel swing cable interference. (c) Half-bar: 80-pixel swing cable interference. (d) Half-bar: 160-pixel swing cable interference. (e) Half-bar: 320-pixel swing cable interference. (f) Half-bar: 640-pixel swing cable interference.

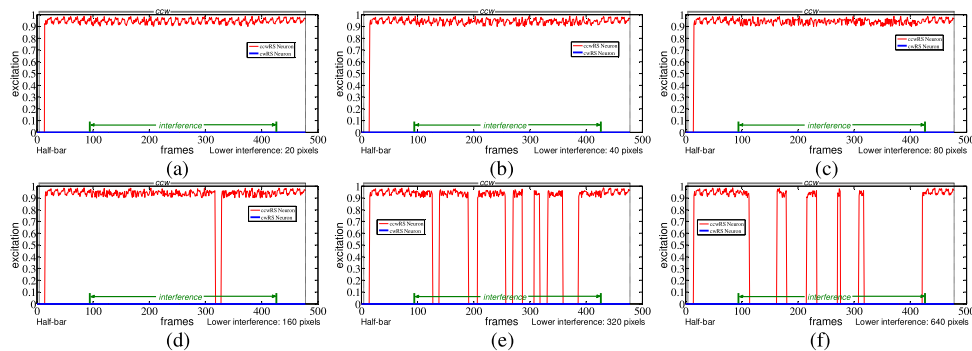


Fig. 24. Output curves of ccwRS neuron and cwRS neuron excitations. Each subgraph uniquely corresponds to the experimental results of a video sequence in Fig. 21(c). (a) Half-bar: 20-pixel swing cable interference. (b) Half-bar: 40-pixel swing cable interference. (c) Half-bar: 80-pixel swing cable interference. (d) Half-bar: 160-pixel swing cable interference. (e) Half-bar: 320-pixel swing cable interference. (f) Half-bar: 640-pixel swing cable interference.

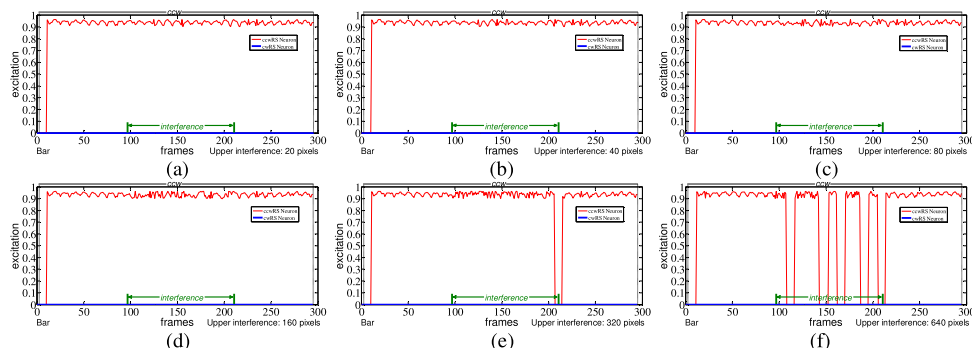


Fig. 25. Output curves of ccwRS neuron and cwRS neuron excitations. Each subgraph uniquely corresponds to the experimental results of a video sequence in Fig. 21(d). (a) Bar: 20-pixel swing cable interference. (b) Bar: 40-pixel swing cable interference. (c) Bar: 80-pixel swing cable interference. (d) Bar: 160-pixel swing cable interference. (e) Bar: 320-pixel swing cable interference. (f) Bar: 640-pixel swing cable interference.

in Fig. 15, and the example frames of each video sequence are shown in Fig. 16.

The rotational motion patterns in ccw of a *half-bar* and a *bar* also are similar to those of the previous simulated visual stimuli generated by a computer except for the difference in the rotation angular velocities (13.46–23.55 rad/s in these types of tests). Figs. 17 and 18 show the experimental results in these tests. From these experimental results, we can see that when the sight axis deviation angle is small up to 30°, the RMPNN can correctly perceive the rotational motion of a half-bar and a bar. This suggests that the RMPNN is robust

to small perturbation in terms of rotational planes. However, with the high increase in the sight axis deviation angle [60° in the video sequence shown in Fig. 16(d) and 45° deg in the video sequence shown in Fig. 16(i)], the perception success rate of the ccwRS neuron began to decline. When the sight axis is almost parallel to the frontoparallel plane, the perception success rate of ccwRS neuron reduced to the minimum and the false alarm rate of cwRS neuron reached to the maximum (see Fig. 18).

**4) Varied Intensity Interference Tests:** In order to test the interference influence on the RMPNN, a set of video

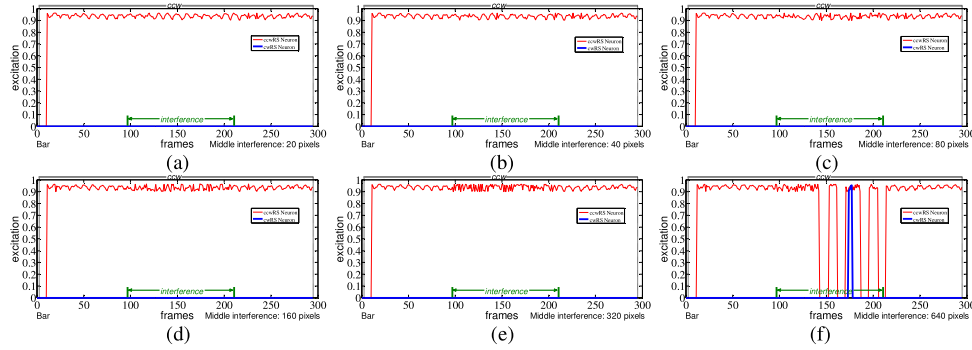


Fig. 26. Output curves of ccwRS neuron and cwRS neuron excitations. Each subgraph uniquely corresponds to the experimental results of a video sequence in Fig. 21(e). (a) Bar: 20-pixel swing cable interference. (b) Bar: 40-pixel swing cable interference. (c) Bar: 80-pixel swing cable interference. (d) Bar: 160-pixel swing cable interference. (e) Bar: 320-pixel swing cable interference. (f) Bar: 640-pixel swing cable interference.

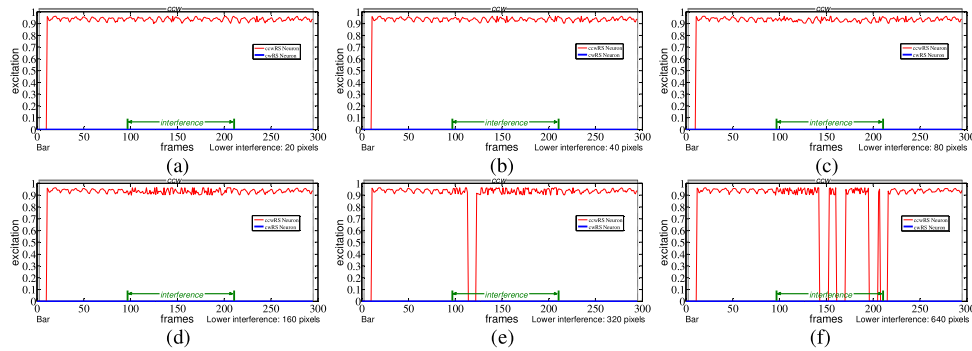


Fig. 27. Output curves of ccwRS neuron and cwRS neuron excitations. Each subgraph uniquely corresponds to the experimental results of a video sequence in Fig. 21(f). (a) Bar: 20-pixel swing cable interference. (b) Bar: 40-pixel swing cable interference. (c) Bar: 80-pixel swing cable interference. (d) Bar: 160-pixel swing cable interference. (e) Bar: 320-pixel swing cable interference. (f) Bar: 640-pixel swing cable interference.

sequences about varied intensity interference scenes was created with a swing black headphone cable. We recorded two original video sequences with a *half-bar* and a *bar* rotating in ccw from the first frame to the end, respectively. In the intermediate time section of each video sequence, a vertical black headphone cable is located on the left side of the rotating object, as interference in the field of view, simulating a pendulum swinging to affect the rotational motion perception of the RMPNN (see Fig. 19). In each of the two video sequences, the cable initially remains stationary for a few seconds and then swings around for several seconds before rests. We then use After Effects CS4 to erase the whole cable to obtain two noninterference rotational motion video sequences of a half-bar and a bar, respectively. Similarly, we get different intensity and swing amplitude interferences in different regions by erasing different parts (upper, middle, and lower) of the cable, as shown in Fig. 21.

The resolution of each original video sequence is 720 pixels. The cable was partially erased and retained different height pixels in the three sections, respectively, forming eight types of interferences of different cable lengths: 0 pixel (the cable disappears completely, i.e., noninterference), 20 pixels, 40 pixels, 80 pixels, 160 pixels, 320 pixels, 640 pixels, and 720 pixels (the full cable remains) (see Figs. 19 and 21).

In these video sequences, all rotational motion patterns of the half-bar and the bar are similar except for the different

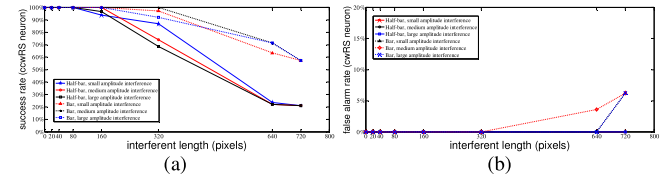


Fig. 28. ccwRS neuron perception success rate and cwRS neuron false alarm rate curves in the varied intensity interference tests. (a) Perception success rates of the ccwRS neuron. (b) Perception false alarm rate of the cwRS neuron.

lengths of the cable interferences. In the half-bar rotation video sequences, each video sequence has 478 frames. A half-bar rotates in ccw at an angular velocity (15.7 rad/s) throughout the whole video sequence. The cable keeps stationary state from frame 1 to frame 94, and then it simulates the pendulum swinging motion from frame 95 to frame 426 and after that it stops swinging and holds still from frame 427 to frame 478. Similarly, each video sequence of a bar rotation has 296 frames. A bar rotates in ccw at an angular velocity (20.93 rad/s) throughout the whole video sequence. The cable keeps stationary state from frame 1 to frame 97, and then it simulates the pendulum swinging around motion from frame 98 to frame 209 and after that it stops swinging and holds still from frame 210 to the last frame.

The performance of the RMPNN against two test results, i.e., the 0-pixel interference (i.e., the cable



Fig. 29. Example frames from the nonrotational motion tests. Each video sequence is represented with five frames; the frame number is indicated under each image. (a) Ball is approaching to the video camera. (b) Ball is receding from the video camera.

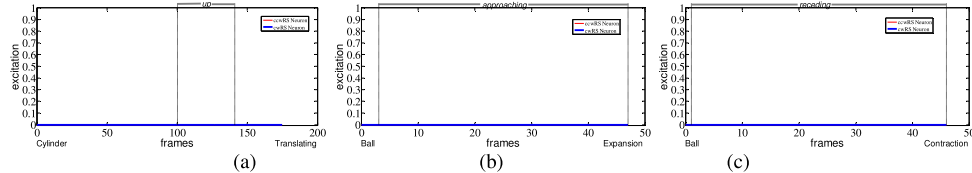


Fig. 30. Output curves of the ccwRS neuron and cwRS neuron excitations in the nonrotational motion tests. Each subgraph uniquely corresponds to the experimental results of a video sequence in these tests. (a) Experimental results corresponding to the video sequences shown in Fig. 2(a). (b) Experimental results corresponding to the video sequences shown in Fig. 29(a). (c) Experimental results corresponding to the video sequences shown in Fig. 29(b).

disappears completely) and the 720-pixel interference (i.e., the full cable remains), is shown in Fig. 20. The other test results of the remaining varied intensity interferences of video sequences are shown in Figs. 22–27, respectively. We also counted the perception success rates of the ccwRS neuron and the false alarm rates of the cwRS neuron in these types of experiments and plotted the rate–interference curves, as shown in Fig. 28. From these tests results, we can find that the proposed RMPNN is robust, as small intensity of interference did not affect its performance. However, its performance will decrease as the strength of interference increases.

5) *Nonrotational Motion Tests*: To see the selectiveness of the RMPNN, we will challenge it with three different types of *nonrotational* motion video sequences. One type is upward translation, the second one is expansion motion, and the third is contraction motion. In Fig. 2(a), a white cylinder is moving upward. In Fig. 29(a), a ball is approaching to the camera. In Fig. 29(b), a ball is receding from the camera.

The test results are shown in Fig. 30. As shown in the Fig. 30(a)–(c), the RMPNN has no response to these nonrotational motions, showing excellent selectiveness of the proposed rotation selective neural network.

#### D. Discussions

In the above sections, the presented RMPNN has been tested using several types of rotational motion video sequences under various conditions. All of these experiments have demonstrated that the RMPNN has a reliable ability to perceive rotational motion. The experimental results showed that the properties of the RMPNN coincide with most of the main functional properties of RS neurons in a monocular viewing condition [6], [43], [44], including rotational motion selective, rotation direction selective, response delay, position invariant, and no preference for nonrotational basic motion (translation, expansion, and contraction).

However, the proposed RMPNN will not respond to the rotational motion in the sagittal plane [43]. The RMPNN is a monocular visual system and it cannot deal with the rotating object in the sagittal plane. This is because the projection of a rotating object, e.g., a bar in the sagittal plane, onto the

field of view will form a periodically expanding/contracting line in a monocular visual system. A binocular vision system with two RMPNNs may still be able to recognize the rotating object, even if a bar may be in the sagittal plane to one of the RMPNNs, given the distances between the two RMPNNs is large enough to allow the other RMPNNs having adequate angle to perceive the rotation (see Figs. 16–18).

The proposed RMPNN contains only 16 direction selective neurons. With this low spatial angular resolution (about  $22.5^\circ$  each and 16 DSNNs to cover the full circle), it can only cope with rotational motion within a certain range of angular velocities. This means that the RMPNN can perceive rotational motion at appropriate rotation speeds effectively but may not respond well to those with too slowly or too fast angular velocities.

The neurophysiological study showed that RS neurons can be classified into three categories according to their responding behaviors to the size of rotational objects [43]. Sakata *et al.*'s [43] experiments showed that most of these types of RS neuron responses increase with the increase in object size, though each type with different size preferences. We examined the influence of object size on the performance of the RMPNN by placing the object with varied distance before the camera. Five separate tests were conducted with distances at 30, 37, 49, 72, and 106 cm, respectively [see Fig. 31(a)]. From these sampled video sequences, we can see that a *half-bar* in the field of view is getting smaller and smaller as the object distance increases. As shown in Fig. 31(b), within a certain range, the change of object distance (i.e., object size) stimulated a similar performance pattern compared with [43] to the RMPNN—the perception success rate increases with the increase in objects size (i.e., closer distance). As detailed in Section III and demonstrated with experiments (Figs. 9–11), the inhibition radius predefined in an RMPNN can affect its preference to different object sizes. This suggests that a population of RMPNNs with different inhibition radii could exhibit a variety of object size preferences for complex visual scenarios.

In our experiments, the original data fed to the RMPNN are the frames extracted from video sequences. Hence, the video

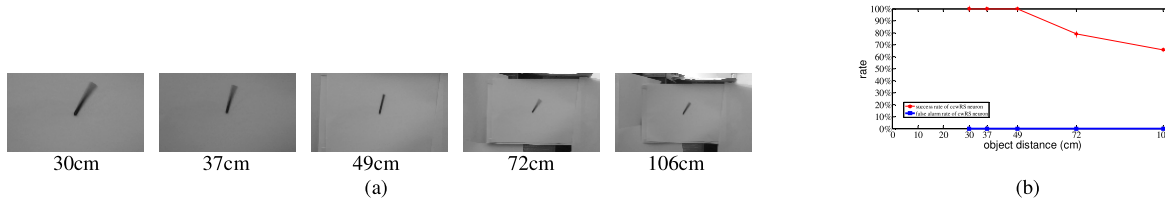


Fig. 31. Varied object distance tests. (a) Example frames from the different object distance tests. Each video sequence is represented with one frame; the object distance is indicated under each image. (b) Perception success rates of the ccwRS neuron curve and the false alarm rates of cwRS neuron curve in the varied object distance tests.

quality (e.g., video definition, data rate, frame rate, and so on) has a significant influence on the performance of the RMPNN if in a real-time application. The key of video technology is video encoding, which directly affects the level of video quality. We hope that in the future work, High Efficiency Video Coding can be introduced to the real-time data acquisition loop of the visual information processing system to effectively improve the efficiency of video encoding, to reduce the corresponding computational complexity [64]–[67], and to enhance the performance of the RMPNN.

## V. CONCLUSION

In the above sections, we proposed a new rotation selective visual neural network, RMPNN, with a specialized spatiotemporal information processing mechanism based on asymmetrically inhibited direction selective neuron models. The direction selective neurons are arranged in a specific order similar to that of the directional columns in the cerebral cortex for perceiving the specific rotational motion cues. Systematic experiments demonstrated that the performance of the proposed RMPNN is robust to position invariance, sight axis deviation, certain range of rotation velocities, and various interferences and object sizes. These characters are consistent with those features of RS neurons revealed in neurophysiological studies [5], [6], [8], [10], [11], [21], [43]. The RMPNN has also demonstrated robust rotation selectiveness of the RMPNN when challenged with nonrotational principle motion patterns (e.g., translation, expansion, and contraction) in our experiments. As the first bio-plausible computational model for rotational motion perception, this research is a significant step toward deep understanding of dynamic visual information processing in both biological and artificial vision systems.

In the future, we may expand our investigation of the perception of rotational motion in 3-D space with binocular RMPNN. The RMPNN may also combine with other types of neurons, to perceive complex motion patterns in the real world.

## ACKNOWLEDGMENT

The authors would like to thank the anonymous reviewers for their valuable comments and the editors of this paper for their kind support. They would also thank Mr. C. Hu for his help in video recording for the experiments.

## REFERENCES

- J. J. Koenderink and A. J. van Doorn, "Local structure of movement parallax of the plane," *J. Opt. Soc. Amer.*, vol. 66, no. 7, pp. 717–723, 1976.
- A. Verri, F. Girosi, and V. Torre, "Differential techniques for optical flow," *J. Opt. Soc. Amer. A*, vol. 7, no. 5, pp. 912–922, 1990.
- D. H. Hubel and T. N. Wiesel, "Receptive fields, binocular interaction and functional architecture in the cat's visual cortex," *J. Physiol.*, vol. 160, no. 1, pp. 106–154, 1962.
- J. H. Maunsell and D. C. Van Essen, "Functional properties of neurons in middle temporal visual area of the macaque monkey. I. Selectivity for stimulus direction, speed, and orientation," *J. Neurophysiol.*, vol. 49, no. 5, pp. 1127–1147, 1983.
- H. Sakata, H. Shibutani, K. Kawano, and T. L. Harrington, "Neural mechanisms of space vision in the parietal association cortex of the monkey," *Vis. Res.*, vol. 25, no. 3, pp. 453–463, 1985.
- H. Sakata, H. Shibutani, Y. Ito, and K. Tsurugai, "Parietal cortical neurons responding to rotary movement of visual stimulus in space," *Experim. Brain Res.*, vol. 61, no. 3, pp. 658–663, 1986.
- K. Tanaka, K. Hikosaka, H. Saito, M. Yukie, Y. Fukada, and E. Iwai, "Analysis of local and wide-field movements in the superior temporal visual areas of the macaque monkey," *J. Neurosci.*, vol. 6, no. 1, pp. 134–144, 1986.
- K. Tanaka and H. Saito, "Analysis of motion of the visual field by direction, expansion/contraction, and rotation cells clustered in the dorsal part of the medial superior temporal area of the macaque monkey," *J. Neurophysiol.*, vol. 62, no. 3, pp. 626–641, 1989.
- R. H. Wurtz, D. S. Yamasaki, C. J. Duffy, and J.-P. Roy, "Functional specialization for visual motion processing in primate cerebral cortex," in *Proc. Cold Spring Harbor Symp. Quant. Biol.*, vol. 55, 1990, pp. 717–727.
- C. J. Duffy and R. H. Wurtz, "Sensitivity of MST neurons to optic flow stimuli. I. A continuum of response selectivity to large-field stimuli," *J. Neurophysiol.*, vol. 65, no. 6, pp. 1329–1345, 1991.
- C. J. Duffy and R. H. Wurtz, "Sensitivity of MST neurons to optic flow stimuli. II. Mechanisms of response selectivity revealed by small-field stimuli," *J. Neurophysiol.*, vol. 65, no. 6, pp. 1346–1359, 1991.
- M. S. Graziano, R. A. Andersen, and R. J. Snowden, "Tuning of MST neurons to spiral motions," *J. Neurosci.*, vol. 14, no. 1, pp. 54–67, 1994.
- L. Lagae, H. Maes, S. Raiguel, D. K. Xiao, and G. A. Orban, "Responses of macaque STS neurons to optic flow components: A comparison of areas MT and MST," *J. Neurophysiol.*, vol. 71, no. 5, pp. 1597–1626, 1994.
- R. D. Santer, P. J. Simmons, and F. C. Rind, "Gliding behaviour elicited by lateral looming stimuli in flying locusts," *J. Comparative Physiol. A*, vol. 191, no. 1, pp. 61–73, 2005.
- R. D. Santer, Y. Yamawaki, F. C. Rind, and P. J. Simmons, "Motor activity and trajectory control during escape jumping in the locust *Locusta migratoria*," *J. Comparative Physiol. A*, vol. 191, no. 10, pp. 965–975, 2005.
- A. D. Huberman, W. Wei, J. Elstrott, B. K. Stafford, M. B. Feller, and B. A. Barres, "Genetic identification of an On-Off direction-selective retinal ganglion cell subtype reveals a layer-specific subcortical map of posterior motion," *Neuron*, vol. 62, no. 3, pp. 327–334, 2009.
- H. Fotowat and F. Gabbiani, "Collision detection as a model for sensory-motor integration," *Annu. Rev. Neurosci.*, vol. 34, no. 1, pp. 1–19, 2011.
- A. Cruz-Martín *et al.*, "A dedicated circuit links direction-selective retinal ganglion cells to the primary visual cortex," *Nature*, vol. 507, no. 7492, pp. 358–361, 2014.
- L. Leinonen, "Functional properties of neurones in the posterior part of area 7 in awake monkey," *Acta Physiol. Scand.*, vol. 108, no. 3, pp. 301–308, 1980.
- G. Rizzolatti, C. Scandolara, M. Matelli, and M. Gentilucci, "Afferent properties of periarcuate neurons in macaque monkeys. II. Visual responses," *Behavioural Brain Res.*, vol. 2, no. 2, pp. 147–163, 1981.

- [21] H. Saito, M. Yukie, K. Tanaka, K. Hikosaka, Y. Fukada, and E. Iwai, "Integration of direction signals of image motion in the superior temporal sulcus of the macaque monkey," *J. Neurosci.*, vol. 6, no. 1, pp. 145–157, 1986.
- [22] P. Cavanagh and O. E. Favreau, "Motion aftereffect: A global mechanism for the perception of rotation," *Perception*, vol. 9, no. 2, pp. 175–182, 1980.
- [23] J. T. Petersik, A. Shepard, and R. Malsch, "A three-dimensional motion aftereffect produced by prolonged adaptation to a rotation simulation," *Perception*, vol. 13, no. 4, pp. 489–497, 1984.
- [24] M. Hershenson, "Visual system responds to rotational and size-change components of complex proximal motion patterns," *Perception Psychophys.*, vol. 42, no. 1, pp. 60–64, 1987.
- [25] M. B. Wall, A. Lingnau, H. Ashida, and A. T. Smith, "Selective visual responses to expansion and rotation in the human MT complex revealed by functional magnetic resonance imaging adaptation," *Eur. J. Neurosci.*, vol. 27, no. 10, pp. 2747–2757, 2008.
- [26] M. C. Morrone, M. Tosetti, D. Montanaro, A. Fiorentini, G. Cioni, and D. C. Burr, "A cortical area that responds specifically to optic flow, revealed by fMRI," *Nature Neurosci.*, vol. 3, no. 12, pp. 1322–1328, 2000.
- [27] A. Koban and R. Cook, "Rotational object discrimination by pigeons," *J. Experim. Psychol., Animal Behavior Process.*, vol. 35, no. 2, pp. 250–265, 2009.
- [28] J. F. Nankoo, C. R. Madan, M. L. Spetch, and D. R. Wyllie, "Perception of complex motion in humans and pigeons (*Columba livia*)," *Experim. Brain Res.*, vol. 232, no. 6, pp. 1843–1853, 2014.
- [29] J. A. Marshall, "Self-organizing neural networks for perception of visual motion," *Neural Netw.*, vol. 3, no. 1, pp. 45–74, 1990.
- [30] F. C. Rind and D. I. Bramwell, "Neural network based on the input organization of an identified neuron signaling impending collision," *J. Neurophysiol.*, vol. 75, no. 3, pp. 967–985, 1996.
- [31] T. Tversky and R. Miikkulainen, "Modeling directional selectivity using self-organizing delay-adaptation maps," *Neurocomputing*, vols. 44–46, pp. 679–684, Jun. 2002.
- [32] S. Yue and F. C. Rind, "Collision detection in complex dynamic scenes using an LGMD-based visual neural network with feature enhancement," *IEEE Trans. Neural Netw.*, vol. 17, no. 3, pp. 705–716, May 2006.
- [33] Z. Zhang, S. Yue, and G. Zhang, "Fly visual system inspired artificial neural networks for collision detection," *Neurocomputing*, vol. 153, pp. 221–234, Apr. 2015.
- [34] G. A. Orban *et al.*, "First-order analysis of optical flow in monkey brain," *Proc. Nat. Acad. Sci. USA*, vol. 89, no. 7, pp. 2595–2599, Apr. 1992.
- [35] I. K. King, J.-S. Liaw, and M. A. Arbib, "A neural network for the detection of rotational motion," in *Proc. Int. Joint Conf. Neural Netw. (IJCNN)*, vol. 1. Seattle, WA, USA, 1991, pp. 707–712.
- [36] A. Guo, H. Sun, and X. Yang, "A multilayer neural network model for perception of rotational motion," *Sci. China C, Life Sci.*, vol. 40, no. 1, pp. 90–100, 1997.
- [37] M. I. Sereno and M. E. Sereno, "Learning to see rotation and dilation with a Hebb rule," in *Proc. Adv. Neural Inf. Process. Syst.*, vol. 3. 1991, pp. 320–326.
- [38] K. Zhang, M. I. Sereno, and M. E. Sereno, "Emergence of position-independent detectors of sense of rotation and dilation with Hebbian learning: An analysis," *Neural Comput.*, vol. 5, no. 4, pp. 597–612, 1993.
- [39] S. A. Beardsley and L. M. Vaina, "Computational modelling of optic flow selectivity in MSTd neurons," *Netw., Comput. Neural Syst.*, vol. 9, no. 4, pp. 467–493, 1998.
- [40] S. A. Beardsley, R. L. Ward, and L. M. Vaina, "A neural network model of spiral-planar motion tuning in MSTd," *Vis. Res.*, vol. 43, no. 5, pp. 577–595, 2003.
- [41] E. T. Rolls and S. M. Stringer, "Invariant global motion recognition in the dorsal visual system: A unifying theory," *Neural Comput.*, vol. 19, no. 1, pp. 139–169, 2007.
- [42] W. Yang, L. Zhang, and L. Ma, "Computational model for rotation-invariant perception," in *Proc. 3rd Int. Conf. Natural Comput. (ICNC)*, vol. 2. 2007, pp. 144–148.
- [43] H. Sakata, H. Shibusaki, Y. Ito, K. Tsurugai, S. Mine, and M. Kusunoki, "Functional properties of rotation-sensitive neurons in the posterior parietal association cortex of the monkey," *Experim. Brain Res.*, vol. 101, no. 2, pp. 183–202, 1994.
- [44] H. Sakata, M. Taira, M. Kusunoki, A. Murata, and Y. Tanaka, "The TINS lecture. The parietal association cortex in depth perception and visual control of hand action," *Trends Neurosci.*, vol. 20, no. 8, pp. 350–357, 1997.
- [45] G. P. Caplovitz and P. U. Tse, "V3A processes contour curvature as a trackable feature for the perception of rotational motion," *Cerebral Cortex*, vol. 17, no. 5, pp. 1179–1189, 2007.
- [46] B. Hassenstein and W. Reichardt, "Systemtheoretische Analyse der Zeit-, Reihenfolgen- und Vorzeichenauswertung bei der Bewegungsperzeption des Rüsselkäfers *Chlorophanus*," *Zeitschrift für Naturforschung B*, vol. 11, nos. 9–10, pp. 513–524, 1956.
- [47] H. B. Barlow and W. R. Levick, "The mechanism of directionally selective units in rabbit's retina," *J. Physiol.*, vol. 178, no. 3, pp. 477–504, 1965.
- [48] N. Franceschini, A. Riehle, and A. Le Nestour, "Directionally selective motion detection by insect neurons," in *Facets of Vision*, D. G. Stavenga *et al.*, Ed. Berlin, Germany: Springer, 1989, pp. 360–390.
- [49] F. C. Rind, "A directionally selective motion-detecting neurone in the brain of the locust: Physiological and morphological characterization," *J. Experim. Biol.*, vol. 149, no. 1, pp. 1–19, 1990.
- [50] F. C. Rind, "Identification of directionally selective motion-detecting neurones in the locust lobula and their synaptic connections with an identified descending neurone," *J. Experim. Biol.*, vol. 149, no. 1, pp. 21–43, 1990.
- [51] A. Borst and J. Haag, "Neural networks in the cockpit of the fly," *J. Comparative Physiol. A*, vol. 188, no. 6, pp. 419–437, 2002.
- [52] S. I. Fried, T. A. Münch, and F. S. Werblin, "Mechanisms and circuitry underlying directional selectivity in the retina," *Nature*, vol. 420, no. 6914, pp. 411–414, 2002.
- [53] N. J. Priebe and D. Ferster, "Direction selectivity of excitation and inhibition in simple cells of the cat primary visual cortex," *Neuron*, vol. 45, no. 1, pp. 133–145, 2005.
- [54] R. Kanjhan and B. Sivyer, "Two types of ON direction-selective ganglion cells in rabbit retina," *Neurosci. Lett.*, vol. 483, no. 2, pp. 105–109, 2010.
- [55] J. P. Gabriel, C. A. Trivedi, C. M. Maurer, S. Ryu, and J. H. Bollmann, "Layer-specific targeting of direction-selective neurons in the zebrafish optic tectum," *Neuron*, vol. 76, no. 6, pp. 1147–1160, 2012.
- [56] W. E. Reichardt and R. W. Schlägl, "A two dimensional field theory for motion computation: First order approximation; translatory motion of rigid patterns," *Biol. Cybern.*, vol. 60, no. 1, pp. 23–35, 1988.
- [57] S. Yue and F. C. Rind, "Visual motion pattern extraction and fusion for collision detection in complex dynamic scenes," *Comput. Vis. Image Understand.*, vol. 104, no. 1, pp. 48–60, Oct. 2006.
- [58] S. Yue and F. C. Rind, "A synthetic vision system using directionally selective motion detectors to recognize collision," *Artif. Life*, vol. 13, no. 2, pp. 93–122, 2007.
- [59] S. Yue and F. C. Rind, "Postsynaptic organisations of directional selective visual neural networks for collision detection," *Neurocomputing*, vol. 103, pp. 50–62, Mar. 2013.
- [60] S. Yue and F. C. Rind, "Redundant neural vision systems—Competing for collision recognition roles," *IEEE Trans. Auton. Mental Develop.*, vol. 5, no. 2, pp. 173–186, Jun. 2013.
- [61] T. D. Albright, R. Desimone, and C. G. Gross, "Columnar organization of directionally selective cells in visual area MT of the macaque," *J. Neurophysiol.*, vol. 51, no. 1, pp. 16–31, 1984.
- [62] M. C. Morrone, D. C. Burr, and L. M. Vaina, "Two stages of visual processing for radial and circular motion," *Nature*, vol. 376, no. 6540, pp. 507–509, 1995.
- [63] S. Yue, F. C. Rind, M. S. Keil, J. Cuadri, and R. Stafford, "A bio-inspired visual collision detection mechanism for cars: Optimisation of a model of a locust neuron to a novel environment," *Neurocomputing*, vol. 69, nos. 13–15, pp. 1591–1598, 2006.
- [64] C. Yan *et al.*, "A highly parallel framework for HEVC coding unit partitioning tree decision on many-core processors," *IEEE Signal Process. Lett.*, vol. 21, no. 5, pp. 573–576, May 2014.
- [65] C. Yan *et al.*, "Efficient parallel framework for HEVC motion estimation on many-core processors," *IEEE Trans. Circuits Syst. Video Technol.*, vol. 24, no. 12, pp. 2077–2089, Dec. 2014.
- [66] C. Yan, Y. Zhang, F. Dai, J. Zhang, L. Li, and Q. Dai, "Efficient parallel HEVC intra-prediction on many-core processor," *Electron. Lett.*, vol. 50, no. 11, pp. 805–806, 2014.
- [67] C. Yan, Y. Zhang, F. Dai, X. Wang, L. Li, and Q. Dai, "Parallel deblocking filter for HEVC on many-core processor," *Electron. Lett.*, vol. 50, no. 5, pp. 367–368, Feb. 2014.



**Bin Hu** received the B.Eng. degree from Central South University, Changsha, China, in 2000, and the M.Eng. degree from Guizhou University, Guiyang, China, in 2007, where he is currently pursuing the Ph.D. degree with the College of Computer Science and Technology.

He has been a Research Assistant with the Computational Intelligence Laboratory, University of Lincoln, U.K., where he was involved in biological visual neural network. He is currently an Associate Professor with the College of Computer Science and Technology, Guizhou University. His current research interests include biological visual neural systems, computer vision, artificial intelligence, and software engineering.



**Zhuhong Zhang** received the M.Sc. degree from Guizhou University, Guiyang, China, in 1998, and the Ph.D. degree from College of Automation, Chongqing University, Chongqing, China, in 2004.

He is currently a Professor with the Guizhou University and an Associate Editor of the *Journal of Applied Soft Computing*. He has authored over 50 journal and conference papers in control theory, intelligent computing, project planning management, and neural network. His current research interests include uncertain programming, evolutionary algorithms, immune optimization, and signal simulation.



**Shigang Yue** (M'05) received the B.Eng. degree from the Qingdao University of Technology, Qingdao, China, in 1988, and the M.Sc. and Ph.D. degrees from the Beijing University of Technology (BJUT), Beijing, China, in 1993 and 1996, respectively.

He was with BJUT as a Lecturer from 1996 to 1998 and an Associate Professor from 1998 to 1999. He was a Senior Research Assistant with Manufacturing Engineering and Engineering Management, City University of Hong Kong, from 1998 to 1999. He was an Alexander von Humboldt Research Fellow from 2000 to 2001 with the University of Kaiserslautern, Kaiserslautern, Germany. He held research positions with University College London, U.K., from 2002 to 2003, Newcastle University, U.K., from 2003 to 2006, and the University of Cambridge, U.K., from 2006 to 2007. He joined the University of Lincoln, U.K., as a Senior Lecturer in 2007, where he was promoted to Reader in 2010, and Professor in 2012. He is currently a Professor with the School of Computer Science, University of Lincoln. He is particularly interested in biological visual neural systems and their applications in unmanned ground/aerial vehicles, interactive systems, and robotics. He has authored over one hundred journal and conference papers in the above research areas. His current research interests include artificial intelligence, computer vision, robotics, brains, and neuroscience.

Prof. Yue is a member of INNS and ISBE. He is the Founding Director of the Computational Intelligence Laboratory in Lincoln and the Deputy Director of the Lincoln Center for Autonomous Systems. He was a Guest Professor in XJTU from 2014 to 2017. He is the coordinator for several EU FP7 and Horizon 2020 projects.